International Journal of Thermofluids 26 (2025) 101081

Contents lists available at ScienceDirect

International Journal of Thermofluids

journal homepage: www.sciencedirect.com/journal/international-journal-of-thermofluids

Investigation of hydro-thermal behavior of two immiscible fluids in a wavy cavity subjected to an inclined magnetic field and heat flux

Mohamed F. Al-Dawody [a], Ahmed M. Hassan [a,*], Nasser H. Hamza [a], Maathe A. Theeb [b], Mohammad Ghalambaz [c,d], Mikhail Sheremet [d]

[a] Mechanical Engineering Department, University of Al-Qadisiyah, Al-Diwaniyah, 58001, Iraq
[b] Mechanical Engineering Department, Mustansiriyah University, Baghdad, 10052, Iraq
[c] Department of Mathematics, Saveetha School of Engineering, SIMATS, Chennai, India
[d] Laboratory on Convective Heat and Mass Transfer, Tomsk State University, 634050, Tomsk, Russia

ARTICLE INFO

Keywords:
Heat transfer
Nanofluid
Immiscible fluids
Cavity
Heat flux
MHD

ABSTRACT

This study investigates the hydro-thermal behavior of two immiscible fluids in a wavy cavity subjected to an inclined magnetic field and heat flux. The cavity contains a nanofluid layer beneath an air layer, with partial bottom heating and cooled vertical walls. The effects of Rayleigh number (*Ra: 10^3–10^6*), wave amplitude (w_a: *0.01–0.15*), wave number (w_n: *0–6*), Hartmann number (*Ha: 0–50*), magnetic field inclination (γ: 0°-90°), and nanoparticle concentration (φ: *0–0.1*) are examined. Results show that increasing *Ra* enhances heat transfer significantly, with Nu_{av} rising by 203 % from $Ra = 10^3$ *to* 10^6. Wall waviness effects are more pronounced at lower *Ra*, while magnetic fields suppress heat transfer at higher *Ra*. Nanoparticle addition enhances heat transfer, particularly at higher *Ra*. The study concludes that optimizing cavity geometry, magnetic field parameters, and nanoparticle concentration can significantly improve heat transfer efficiency, especially at higher *Ra*. These findings provide valuable insights for designing efficient thermal management solutions in various industrial applications.

1. Introduction

Heat transfer technology, whether forced or natural, plays a crucial role in engineering and industrial applications. However, both mechanical engineers and academic researchers always strive to find the best compromise scenario between maximum thermal efficiency and minimum power consumption. Cavity or enclosure is one of the most common physical confining geometries that can be found in many applications, such as solar collectors [1,2], electronic device coolers [3], passive cooling techniques [4], and so on. Consequently, numerous studies investigate cavities of various types, geometric configurations, and operating conditions.

The basic geometry of a cavity is the square, which has been studied by numerous researchers, to name but a few [5–7]. It had been studied considering different working fluids [8,9], orientation and boundary conditions [10,11] and all other possible modifications. Studies extended to consider different regular shapes like rectangular [12,13], triangular [14,15], circular [16,17], trapezoidal [18–20], elliptical [21,22], octagonal [23,24], etc. Also, irregular or combined geometries have been investigated like I-shape [25,26], H-shape [27–29], E-shape [30,31] etc. It is worth mentioning that all the aforementioned geometries are tested at different operating conditions like laminar or turbulent flows and different working fluids starting from low Prandtl number fluids to high ones.

A cavity with a corrugated wall or walls was one of interest to researchers due to its merits in altering fluid motion inside the cavity [32]. Haq et al. [33] studied a horizontal waved wall porous cavity influenced by an external magnetic field. They found that the corrugation profile can affect the fluid motion and Nu majorly but it has a minor effect on Da and Ha numbers. On the other hand, Selimefendigil and Öztop found in their study [34] stated that corrugation profile had a negative effect on the quantity of transferred heat although it can enhance HT at low corrugation degree.

Other researchers focus on the effect of applying an external magnetic field to a cavity. Bozhko et al. [35] conducted an experimental study to investigate the effect of an external constant magnetic field on a

* Corresponding author.
E-mail addresses: Mohamed.aldawody@qu.edu.iq (M.F. Al-Dawody), ahmed.mohammed.hassan@qu.edu.iq (A.M. Hassan), naseer.hamza@qu.edu.iq (N.H. Hamza), maathe@uomustansiriyah.edu.iq (M.A. Theeb), m.ghalambaz@gmail.com (M. Ghalambaz), michael-sher@yandex.ru (M. Sheremet).

https://doi.org/10.1016/j.ijft.2025.101081

Available online 14 January 2025

fluid that filled a spherical cavity. They observed that applying a horizontal magnetic field can strongly weaken the convection strength, indicating the impact of magnetic force on heat transfer magnitude. In a similar context, Sheikholeslami et al. [36] numerically simulated the hydrothermal characteristics of an alcohol-based fluid using the Lattice Boltzman method. Their results supported the fact that magnetization has a negative impact on heat transfer. Gangawane [37] studied the effect of the cavity orientation, and he found the maximum negative impact on the natural convection heat transfer inside the cavity can occur when applying a 45-degree magnetic field to the cavity. Dixit and Pattamatta [38], on the other hand, discovered that applying a magnetic field can either decrease or increase the heat transfer rate, depending on the volume fraction of the ferrofluid. Ramesh et al. [39] investigated hybrid Casson nanoliquids under MHD effects, demonstrating that temperature distribution showed positive correlation with both Prandtl and Hartmann numbers, providing valuable insights for thermal management applications. Reddy and Ramesh [40] examined magnetohydrodynamic convective nanofluid flow over a wedge surface, incorporating binary chemical reaction and Arrhenius activation energy, revealing enhanced flow characteristics with increasing wedge angle and temperature ratio parameters. Ramesh [41] studied Ree-Eyring hydromagnetic fluid flows through porous media with slip boundary conditions and thermal radiation effects, though the provided abstract appears to discuss a different topic. Gajbhiye et al. [42] analyzed non-Newtonian fluid flow in microchannels with EMHD and thermal radiation, finding that Darcy number and Casson fluid parameters enhance velocity profiles while radiation parameters suppress temperature profiles.

Recent studies have demonstrated the effectiveness of two-phase Lattice Boltzmann Method (LBM) for modeling nanofluid behavior in enclosures. For example, Abdollahzadeh et al. [43] showed improved prediction accuracy for nanoparticle distribution using LBM. Qi et al. [44,45] demonstrated better capture of interfacial phenomena with two-phase approaches. However, for our specific configuration, where the primary focus is on bulk fluid behavior and overall heat transfer characteristics rather than detailed particle-fluid interactions, the single-phase model provides sufficient accuracy while being computationally more efficient.

There are few studies that are concerned with two superposed immiscible fluids in the same cavity. The problem has direct applications in many industrial and engineering applications where occurrence of two superposed fluid confined together is the practical situation. Oueslati et al. [46] introduced an analytical solution for such problems using a parallel flow approximation and a numerical solution. The study aimed to compare the two models by analyzing the average Nusselt number, as well as the temperature and velocity contours. Liu et al. [47] studied the effects of thermo-gravitational forces and surface tension in several layers of liquid. They used the finite difference method to numerically solve the governing equations with a Boussinesq approximation. Their findings revealed the appearance of typical convection patterns during interfacial tension, which played a critical role in determining them. The research by Ouahouah et al. [48] was mostly about how the dynamic viscosity and thermal diffusivity ratios affect the temperature and stream function patterns in the cavity. The results showed that when the surface tension gradient made the advective transport rate low, the fluid moved from low interfacial tension values to high values more quickly. Salari et al. [49] performed a three-dimensional case study to explore the effect of nanofluid interface aspect ratio on the overall thermal performance of two layers of fluids; the upper was air and the lower was composed of a nano-water-based fluid. The entropy generation was decreased on the other hand with a high Ra number.

The studies on wavy cavity configuration with two immiscible fluid layers have several important industrial and engineering applications. The wavy walls improve heat transfer by giving the fluid more surface area and better mixing. This shape works especially well for small heat exchangers because it improves thermal performance while keeping the size small, which is important for cooling electronics and HVAC systems. In solar thermal collectors, the two-layer system with nanofluids can improve heat absorption and transfer efficiency. The enhanced mixing due to wavy walls is beneficial in chemical processing equipment, specifically in reactors where two immiscible fluids are involved. The magnetic field control offers an additional parameter for regulating heat transfer in industrial cooling systems where electromagnetic fluids are used. The configuration is also applicable in microfluidic devices, particularly in lab-on-chip applications where controlled heat transfer between immiscible fluids is required. Furthermore, the two-layer system can be effectively applied in energy storage systems where phase change materials or heat transfer fluids are utilized for thermal energy storage.

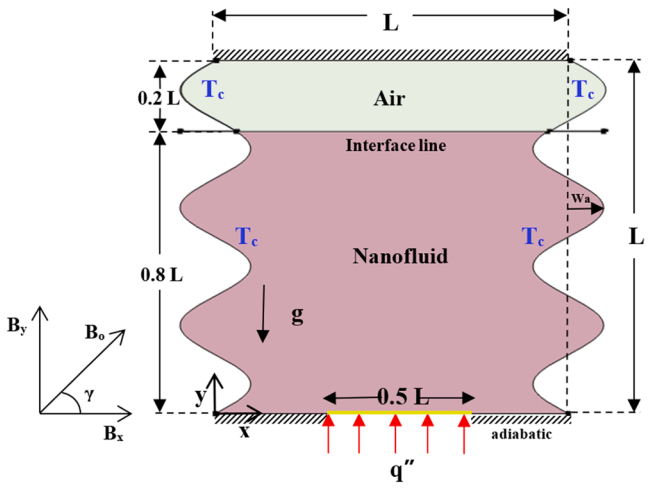

Fig. 1. The geometry of the case study.

A close study of the literature mentioned earlier shows that researchers haven't paid much attention to the problem of having more than one layer of fluid inside an enclosure, especially when it comes to the effects of magnetic fields and wall waviness working together. The present study aims to answer several key research questions: How do wavy walls affect heat transfer in two-layer immiscible fluid systems? What is the impact of an inclined magnetic field on the flow patterns and thermal behavior of such systems? What is the impact of adding nanoparticles on the heat transfer characteristics across the fluid interface?

The novelty of this work lies in its comprehensive investigation of these combined effects, which has not been previously explored. We present the first in-depth study of the thermophysical properties and flow patterns in a two-layer system of immiscible fluids inside a corrugated chamber when an inclined magnetic field is present. The results of this study have significant implications for various practical applications, particularly in desalination chambers where enhanced heat transfer and controlled fluid mixing are crucial for system efficiency.

2. Problem formulation

The considered case of study composes of two immiscible layers of two fluids rested in a cavity as shown in Fig. 1. The upper layer where air is located occupies 0.2 of total depth of the cavity while the lower layer contains a nanofluid that fills the remaining section of the cavity. An interface line isolated them from each other. Heat flux is applied to a partial section of the bottom wall of the cavity, while the rest is insulated as the upper wall. The two vertical wavy walls are kept at the lower temperature of the system T_c. These walls are corrugated with w_n number of waves that their amplitude is extended up to w_a unit of length. The entire system is subjected to an inclined magnetic force that is directed from the outside. The wavy vertical walls follow a sinusoidal

profile described by the equation: $x = A{\cdot}sin\left(2\pi w_n{\cdot}\frac{y}{L}\right)$ where A is the wave amplitude (w_a) varying from 0.01 L to 0.15 L, and w_n is the number of waves (0 to 6). The heated section on the bottom wall extends from $x = 0.25L$ to $x = 0.75L$. The total cavity width L is taken as the characteristic length for non-dimensionalization of the governing equations.

The mathematical model for this study is developed based on several key assumptions. The flow is considered steady-state, laminar, and incompressible, with constant fluid properties except for density in buoyancy terms (Boussinesq approximation). A no-slip condition is assumed at all solid boundaries. Both fluids are treated as Newtonian, with uniformly distributed nanoparticles in the lower layer and temperature-independent thermophysical properties. Heat transfer considerations include negligible viscous dissipation, no radiation effects, stable fluid interface, and thermal equilibrium between nanoparticles and base fluid. For electromagnetic effects, the induced magnetic field is considered negligible compared to the applied field, while electric field effects and Hall effect are neglected. These assumptions are consistent with similar studies in the literature and are valid within the parameter ranges investigated in this work. [50–52].

For air domain continuity equation:

$$\frac{\partial u}{\partial x}+\frac{\partial v}{\partial y}=0. \tag{1}$$

momentum conservation equations:

$$u\frac{\partial u}{\partial x}+v\frac{\partial u}{\partial y}=-\frac{1}{\rho_a}\frac{\partial p}{\partial x}+\nu_a\left[\frac{\partial^2 u}{\partial x^2}+\frac{\partial^2 u}{\partial y^2}\right]+\frac{F_x}{\rho_a} \tag{2}$$

$$u\frac{\partial v}{\partial x}+v\frac{\partial v}{\partial y}=-\frac{1}{\rho_a}\frac{\partial p}{\partial y}+\nu_a\left[\frac{\partial^2 v}{\partial x^2}+\frac{\partial^2 v}{\partial y^2}\right]+\frac{g(\rho\beta)_a}{\rho_a}(T-T_c)+\frac{F_y}{\rho_a} \tag{3}$$

where F_x and F_y are the Lorentz force components. They are defined by [53]:

$$F_x=\sigma_a\,B_0^2\left(vsin\,(\gamma)cos\,(\gamma)-usin^2\,(\gamma)\right) \tag{4}$$

$$F_y=\sigma_a\,B_0^2\left(usin\,(\gamma)cos\,(\gamma)-vcos^2\,(\gamma)\right) \tag{5}$$

where σ_a, B_o, ν_a, ρ_a, and γ are electrical conductivity of air, magnetic field density, kinematic viscosity of air, density of air, and magnetic field inclination angle, respectively. energy equation:

$$u\frac{\partial T}{\partial x}+v\frac{\partial T}{\partial y}=\alpha_a\left[\frac{\partial^2 T}{\partial x^2}+\frac{\partial^2 T}{\partial y^2}\right] \tag{6}$$

where α_a is thermal diffusivity of air.

For nanofluid domain

Continuity equation:

$$\frac{\partial u}{\partial x}+\frac{\partial v}{\partial y}=0 \tag{7}$$

momentum conservation equations [54]:

$$u\frac{\partial u}{\partial x}+v\frac{\partial u}{\partial y}=\ -\frac{1}{\rho_{nf}}\frac{\partial p}{\partial x}+\nu_{nf}\left[\frac{\partial^2 u}{\partial x^2}+\frac{\partial^2 u}{\partial y^2}\right]+\frac{F_x}{\rho_{nf}} \tag{8}$$

$$u\frac{\partial v}{\partial x}+v\frac{\partial v}{\partial y}=-\frac{1}{\rho_{nf}}\frac{\partial p}{\partial y}+\nu_{nf}\left[\frac{\partial^2 v}{\partial x^2}+\frac{\partial^2 v}{\partial y^2}\right]+\frac{g(\rho\beta)_{nf}}{\rho_{nf}}(T-T_c)+\frac{F_y}{\rho_{nf}} \tag{9}$$

where F_x and F_y are the Lorentz force components. The are defined by [53]:

$$F_x=\sigma_{nf}\,B_0^2\left(vsin\,(\gamma)cos\,(\gamma)-usin^2\,(\gamma)\right) \tag{10}$$

$$F_y=\sigma_{nf}\,B_0^2\left(usin(\gamma)cos(\gamma)-vcos^2(\gamma)\right) \tag{11}$$

where σ_{nf}, ν_{nf}, and ρ_{nf} are electrical conductivity of nanofluid, kinematic viscosity of nanofluid, and density of nanofluid, respectively. energy equation [54]:

$$u\frac{\partial T}{\partial x}+v\frac{\partial T}{\partial y}=\alpha_{nf}\left[\frac{\partial^2 T}{\partial x^2}+\frac{\partial^2 T}{\partial y^2}\right] \tag{12}$$

The balance between shear stress, temperature continuity, and heat flux determines the thermal and viscous conditions at the interface of the fluid layers. The boundary conditions at the interface line can be defined as:

$$u_a=u_{nf},\ v_a=v_{nf}=0\ 0\le x\le L,\ y=0.8\ L \tag{13}$$

$$T_a=T_{nf},\ k_a\frac{\partial T_a}{\partial y}=k_{nf}\frac{\partial T_{nf}}{\partial y}\ \rightarrow\frac{k_a}{k_f}\frac{\partial T_a}{\partial y}=\frac{k_{nf}}{k_f}\frac{\partial T_{nf}}{\partial y}\ 0\le x\le L,\ y=0.8\ L \tag{14}$$

Introducing the following parameter in order to get the non-dimensional form of abovementioned governing equations:

$$X=\frac{x}{L},\ Y=\frac{y}{L},\ U=\frac{uL}{\alpha_f},\ V=\frac{vL}{\alpha_f},\ P=\frac{pL^2}{\rho_f\alpha_f^2},\ \theta=\frac{T-T_c}{\Delta T},\ \alpha_{nf}=\frac{k_{nf}}{(\rho C_p)_{nf}},\ Pr=\frac{\nu_f}{\alpha_f},\ Ra=\frac{g\beta(\Delta T)L^3}{a_f\nu_f},\ Ha=B_0L\sqrt{\frac{\sigma}{\mu}},\ \Delta T=\frac{q''L}{k_f}.$$

where Pr, Ra, and Ha are Prandtl number, Rayleigh number, and Hartmann number, respectively. The non-dimensional equations can be written as [49,54]:

For the air layer:

$$\frac{\partial U}{\partial X}+\frac{\partial V}{\partial Y}=0 \tag{15}$$

$$\frac{\rho_a}{\rho_f}\left(U\frac{\partial U}{\partial X}+V\frac{\partial U}{\partial Y}\right)=-\frac{\partial P}{\partial X}+\frac{\mu_a}{\mu_f}Pr\left(\frac{\partial^2 U}{\partial X^2}+\frac{\partial^2 U}{\partial Y^2}\right)+\frac{\mu_a}{\mu_f}PrHa^2\left(V\sin(\gamma)\cos(\gamma)-U\sin^2(\gamma)\right) \tag{16}$$

$$\frac{\rho_a}{\rho_f}\left(U\frac{\partial V}{\partial X}+V\frac{\partial V}{\partial Y}\right)=-\frac{\partial P}{\partial Y}+\frac{\mu_a}{\mu_f}Pr\left(\frac{\partial^2 V}{\partial X^2}+\frac{\partial^2 V}{\partial Y^2}\right)+\frac{(\rho\beta)_a}{(\rho\beta)_f}PrRa\theta+\frac{\mu_a}{\mu_f}\frac{\rho_f}{\rho_a}PrHa^2\left(Usin(\gamma)\cos(\gamma)-V\cos^2(\gamma)\right) \tag{17}$$

$$\frac{(\rho C_p)_a}{(\rho C_p)_f}\left(U\frac{\partial\theta}{\partial X}+V\frac{\partial\theta}{\partial Y}\right)=\frac{k_a}{k_f}\left(\frac{\partial^2\theta}{\partial X^2}+\frac{\partial^2\theta}{\partial Y^2}\right) \tag{18}$$

For the nanofluid layer:

$$\frac{\partial U}{\partial X}+\frac{\partial V}{\partial Y}=0 \tag{19}$$

$$\frac{\rho_{nf}}{\rho_f}\left(U\frac{\partial U}{\partial X}+V\frac{\partial U}{\partial Y}\right)=-\frac{\partial P}{\partial X}+\frac{\mu_{nf}}{\mu_f}Pr\left(\frac{\partial^2 U}{\partial X^2}+\frac{\partial^2 U}{\partial Y^2}\right)+PrHa^2\frac{\sigma_{nf}}{\sigma_f}\left(V\sin(\gamma)\cos(\gamma)-U\sin^2(\gamma)\right) \tag{20}$$

$$\frac{\rho_{nf}}{\rho_f}\left(U\frac{\partial V}{\partial X}+V\frac{\partial V}{\partial Y}\right)=-\frac{\partial P}{\partial Y}+\frac{\mu_{nf}}{\mu_f}Pr\left(\frac{\partial^2 V}{\partial X^2}+\frac{\partial^2 V}{\partial Y^2}\right)+\frac{(\rho\beta)_{nf}}{(\rho\beta)_f}RaPr\theta+PrHa^2\frac{\sigma_{nf}}{\sigma_f}\left(U\sin(\gamma)\cos(\gamma)-V\cos^2(\gamma)\right) \tag{21}$$

$$\frac{(\rho C_p)_{nf}}{(\rho C_p)_f}\left(U\frac{\partial\theta}{\partial X}+V\frac{\partial\theta}{\partial Y}\right)=\frac{k_{nf}}{k_f}\left(\frac{\partial^2\theta}{\partial X^2}+\frac{\partial^2\theta}{\partial Y^2}\right) \tag{22}$$

Generally, the calculation of Nusselt number is based on the heat flux at the wall [49].

Table 1
Thermal-physical properties of water, air, and TiO_2 nanoparticles. [55,56].

	ρ (kg. m^{-3})	C_p(J. kg^{-1}. K^{-1})	k (W. m^{-1}. K^{-1})	β (1/K)	μ (kg. m^{-1}. s^{-1})
Pure water	997.1	4179	0.613	21×10^{-5}	1.003×10^{-3}
TiO_2	4250	686.2	8.95	0.9×10^{-5}	–
Air	1.25	1005	0.0257	3.43×10^{-3}	3.178×10^{-5}

$$Nu(x) = \frac{h(x).L}{K_f}\ ,\ h(x) = \frac{q''}{T - T_c} \rightarrow q'' = \frac{k_f \times \Delta T}{L} \tag{23}$$

By using the dimensionless parameters, and rearranging the local Nusselt number, yields [49]

$$\therefore Nu(X) = \frac{\left(\frac{q''}{T-T_c}\right).L}{K_f} = \frac{L \times K_f \times \Delta T}{K_f \times (T - T_c) \times L} = \frac{\Delta T}{T - T_c} = \frac{1}{\theta(X)} \tag{24}$$

$$Nu_{av} = \frac{1}{L}\int_0^1 Nu(X)dX \tag{25}$$

The enclosure's upper and lower regions were characterized by distinct physical properties corresponding to air and nanofluid, respectively. While air properties remained constant (as detailed in Table 1 [55,56]), the nanofluid's properties varied as functions of the solid volume fraction (ϕ). The key nanofluid properties are defined by the following relationships [2]:

$$\rho_{\mathrm{nf}} = (1 - \phi)\rho_{\mathrm{f}} + \phi\rho_{\mathrm{p}} \tag{26}$$

where ϕ is the nanofluid solid volume fraction. Also, α_{nf} is the thermal diffusivity of the nanofluid and is given by:

$$\alpha_{\mathrm{nf}} = \frac{\mathrm{k_{nf}}}{(\rho \mathrm{Cp})_{\mathrm{nf}}} \tag{27}$$

where $(\rho C_p)_{nf}$ is the specific heat capacity of the nanofluid and it is determined by [57]:

$$(\rho \mathrm{Cp})_{\mathrm{nf}} = (1 - \phi)(\rho \mathrm{Cp})_{\mathrm{f}} + \phi(\rho \mathrm{Cp})_{\mathrm{p}} \tag{28}$$

In addition, $(\rho\beta)_{\mathrm{nf}}$ is the thermal expansion coefficient of the nanofluid and is expressed as:

$$(\rho\beta)_{\mathrm{nf}} = (1 - \phi)(\rho\beta)_{\mathrm{f}} + \phi(\rho\beta)_{\mathrm{p}} \tag{29}$$

Moreover, μ_{nf} is the effective dynamic viscosity of the nanofluid which is given by [2] as:

$$\mu_{\mathrm{nf}} = \frac{\mu_{\mathrm{f}}}{(1 - \phi)^{2.5}} \tag{30}$$

the thermal conductivity of nanofluid $\mathrm{k_{nf}}$ is given by [56]:

$$\mathrm{k_{nf}} = \mathrm{k_f}\left[\frac{(\mathrm{k_p} + 2\mathrm{k_f}) - 2\phi(\mathrm{k_f} - \mathrm{k_p})}{(\mathrm{k_p} + 2\mathrm{k_f}) + \phi(\mathrm{k_f} - \mathrm{k_p})}\right] \tag{31}$$

3. Numerical methodology

The well-known Finite Element using Galerkin method (FEGM) is utilized to solve the governing equations of continuity, momentum, and energy. Using the benefit of the law of mass conservation, the aforementioned Eq. (15) can be used as a constraint to solve the two-components equations of momentum., Eqs. (16) and (17) [58,59]. In this way, Eqs. (16–18) can be solved by introducing penalty parameters η and γ to satisfy the continuity equation:

$$P = -\eta\left(\frac{\partial U}{\partial X} + \frac{\partial V}{\partial Y}\right); where\ \eta = \gamma\frac{\rho_a}{\rho_f} \tag{32}$$

Now using the above equation, the dimensionless momentum equations for upper air layer can be re-written as:

$$U\frac{\partial U}{\partial X} + V\frac{\partial U}{\partial Y} = \eta\frac{\partial}{\partial X}\left(\frac{\partial U}{\partial X} + \frac{\partial V}{\partial Y}\right) + \frac{\nu_a}{\nu_f}Pr\left(\frac{\partial^2 U}{\partial X^2} + \frac{\partial^2 U}{\partial Y^2}\right) + \frac{\nu_a}{\nu_f}PrHa^2\left(V\sin(\gamma)\cos(\gamma) - U\sin^2(\gamma)\right) \tag{33}$$

$$U\frac{\partial U}{\partial X} + V\frac{\partial U}{\partial Y} = \eta\frac{\partial}{\partial X}\left(\frac{\partial U}{\partial X} + \frac{\partial V}{\partial Y}\right) + \frac{\nu_a}{\nu_f}Pr\left(\frac{\partial^2 V}{\partial X^2} + \frac{\partial^2 V}{\partial Y^2}\right) + \frac{\beta_a}{\beta_f}PrRa\theta + \frac{\nu_a}{\nu_f}\frac{\rho_f}{\rho_a}PrHa^2\left(U\sin(\gamma)\cos(\gamma) - V\cos^2(\gamma)\right) \tag{34}$$

Th Galerkin method (FEGM) involves dividing the problem domain Ω into smaller sub-domains and elements Ω^e of the current domain of study. By using of numerical approximation representation $\Xi^i(x,y)$ of any of aforementioned governing equations Ξ(x, y) and utilizing basis functions to approximate the solutions within each of these elements for each unknown parameter ϱ^i.

$$\Xi^i(x,\ y) = \sum_{i=1}^{n}\Lambda^i(x,y)\varrho^i \tag{35}$$

where *n*: unknown parameters; $\Lambda^i(x,y)$: shape function.

The main attention in the current study was directed towards stream function and isotherm at different orientations and operating conditions, thus the velocity components and temperature can be formulated over the subdomain Ω^e:

$$U \approx \sum_{k=1}^{n}\Lambda_k(x,y)U_k,\ V \approx \sum_{i=1}^{n}\Lambda_k(x,y)V_k\ and\ \theta \approx \sum_{i=1}^{n}\Lambda_k(x,y)\theta_k \tag{36}$$

thus the numerical residual can be described briefly over the internal domain Ω for the upper air layer [58,60–62]:

$$R_i^{(1)} = \sum_{k=1}^{n}U_k\int_\Omega\left[\left(\sum_{k=1}^{n}U_k\Lambda_k\right)\frac{\partial\Phi_k}{\partial X} + \left(\sum_{k=1}^{n}V_k\Lambda_k\right)\frac{\partial\Lambda_k}{\partial Y}\right]\Lambda_i\ dX\ dY + \eta$$
$$\left[\sum_{k=1}^{n}U_k\int_\Omega\frac{\partial\Lambda_i}{\partial X}\frac{\partial\Lambda_k}{\partial X}\ dX\ dY + \sum_{k=1}^{n}V_k\int_\Omega\frac{\partial\Lambda_i}{\partial X}\frac{\partial\Lambda_k}{\partial Y}\ dX\ dY + \frac{\nu_a}{\nu_f}Pr\sum_{k=1}^{n}U_k\int_\Omega\left[\frac{\partial\Lambda_i}{\partial X}\frac{\partial\Lambda_k}{\partial X} + \frac{\partial\Lambda_i}{\partial Y}\frac{\partial\Lambda_k}{\partial Y}\right]dX\ dY\right] \tag{37}$$
$$-\frac{\nu_a}{\nu_f}PrHa^2\left[\sin(\gamma)\cos(\gamma)\int_\Omega\left(\sum_{k=1}^{n}V_k\Lambda_k\right)\Lambda_i\ dX\ dY - \sin^2(\gamma)\int_\Omega\left(\sum_{k=1}^{n}U_k\Lambda_k\right)\Lambda_i\ dX\ dY\right]$$

$$R_i^{(2)} = \sum_{k=1}^{n} V_k \int_{\Omega} \left[\left(\sum_{k=1}^{n} U_k \Lambda_k \right) \frac{\partial \Lambda_k}{\partial X} + \left(\sum_{k=1}^{n} V_k \Lambda_k \right) \frac{\partial \Lambda_k}{\partial Y} \right] \Lambda_i \, dX \, dY + \eta$$

$$\left[\sum_{k=1}^{n} U_k \int_{\Omega} \frac{\partial \Lambda_i}{\partial Y} \frac{\partial \Lambda_k}{\partial X} \, dX \, dY + \sum_{k=1}^{n} V_k \int_{\Omega} \frac{\partial \Lambda_i}{\partial Y} \frac{\partial \Lambda_k}{\partial Y} \, dX \, dY \right] + \frac{\nu_a}{\nu_f} Pr \sum_{k=1}^{n} V_k \int_{\Omega} \left[\frac{\partial \Lambda_i}{\partial X} \frac{\partial \Lambda_k}{\partial X} + \frac{\partial \Lambda_i}{\partial Y} \frac{\partial \Lambda_k}{\partial Y} \right] \tag{38}$$

$$dX \, dY - \frac{\beta_a}{\beta_f} PrRa \int_{\Omega} \left(\sum_{k=1}^{n} \theta_k \Lambda_k \right) \Lambda_i \, dX \, dY - \frac{\nu_a}{\nu_f} \frac{\rho_f}{\rho_a} PrHa^2 \left[\sin(\gamma)\cos(\gamma) \int_{\Omega} \left(\sum_{k=1}^{n} U_k \Lambda_k \right) \Lambda_i \, dX \, dY - \cos^2(\gamma) \int_{\Omega} \left(\sum_{k=1}^{n} V_k \Lambda_k \right) \Lambda_i \, dX \, dY \right]$$

And

$$R_i^{(3)} = \sum_{k=1}^{n} \theta_k \int_{\Omega} \left[\left(\sum_{k=1}^{n} U_k \Lambda_k \right) \frac{\partial \Lambda_k}{\partial X} + \left(\sum_{k=1}^{n} V_k \Lambda_k \right) \frac{\partial \Lambda_k}{\partial Y} \right] \Lambda_i \, dX \, dY + \frac{\alpha_{nf}}{\alpha_f} \sum_{k=1}^{n} \theta_k \int_{\Omega} \left[\frac{\partial \Lambda_i}{\partial X} \frac{\partial \Lambda_k}{\partial X} + \frac{\partial \Lambda_i}{\partial Y} \frac{\partial \Lambda_k}{\partial Y} \right] dX \, dY \tag{39}$$

The same procedure can be easily repeated for the lower nanofluid layer.

The Finite Element Method (FEM) was employed to solve the governing equations. The computational domain was discretized using quadrilateral elements, with finer mesh near the walls and interface to capture steep gradients. The solution procedure followed these key steps:

1. Domain Discretization: The cavity was divided into non-uniform quadrilateral elements, with mesh refinement in critical regions. Element size was determined through grid independence testing, showing variations <0.3 % between successive refinements.
2. Interpolation Functions: Second-order Lagrange polynomials were used for velocity components and temperature, while linear functions were employed for pressure. This choice ensures numerical stability and accuracy in capturing both flow and thermal fields.
3. Weak Formulation: The governing equations were converted to their weak form using the Galerkin method. Appropriate weight functions were applied to minimize residuals across the domain.
4. System Solution: The resulting system of algebraic equations was solved iteratively using the Newton-Raphson method. Convergence was achieved when relative residuals fell below 10^{-6} for all variables.

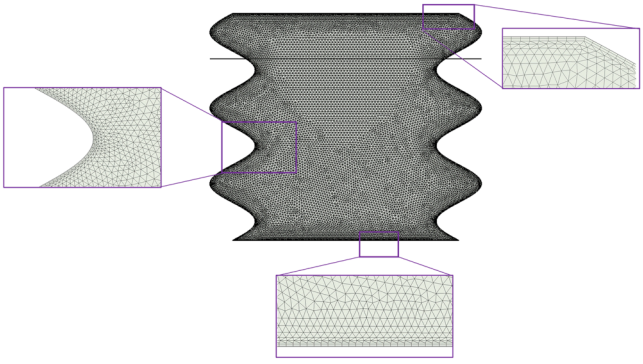

Fig. 2. The discretization of the entire geometry.

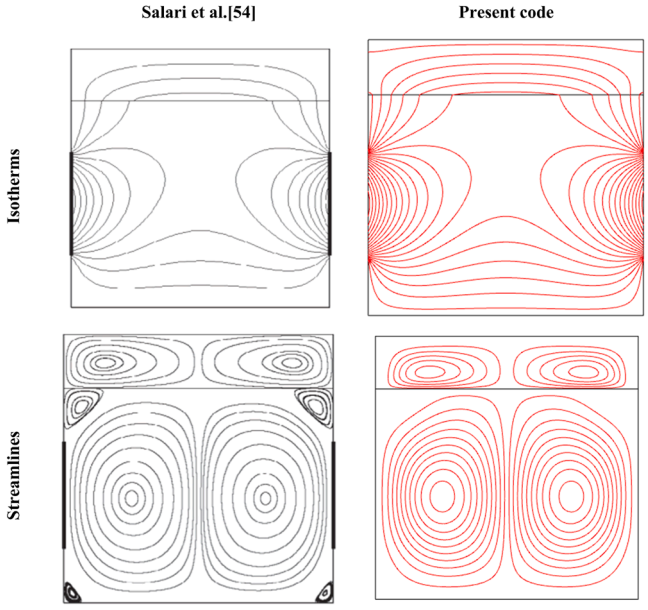

Fig. 3. Comparison of the results between the current study and study of Salari et al. [54]..

Table 2
The grid independence test of different schemes of discretization.

Grid	G1	G2	Deviation	G3	Deviation	G4 (selected grid)	Deviation	G5	Deviation
N^{o} of elements	4063	6061		9128		20,739		28,087	
Ra N^{o}	Nu_{av}	Nu_{av}		Nu_{av}		Nu_{av}		Nu_{av}	
1000	4.5038	4.4949	0.20 %	4.4851	0.22 %	4.4811	0.09 %	4.4799	0.03 %
10,000	4.5481	4.5390	0.20 %	4.5303	0.19 %	4.5267	0.08 %	4.5254	0.03 %
100,000	6.6525	6.6624	0.15 %	6.6584	0.06 %	6.6585	0.00 %	6.6612	0.04 %
1,000,000	12.982	12.976	0.05 %	12.948	0.22 %	12.924	0.19 %	12.924	0.00 %

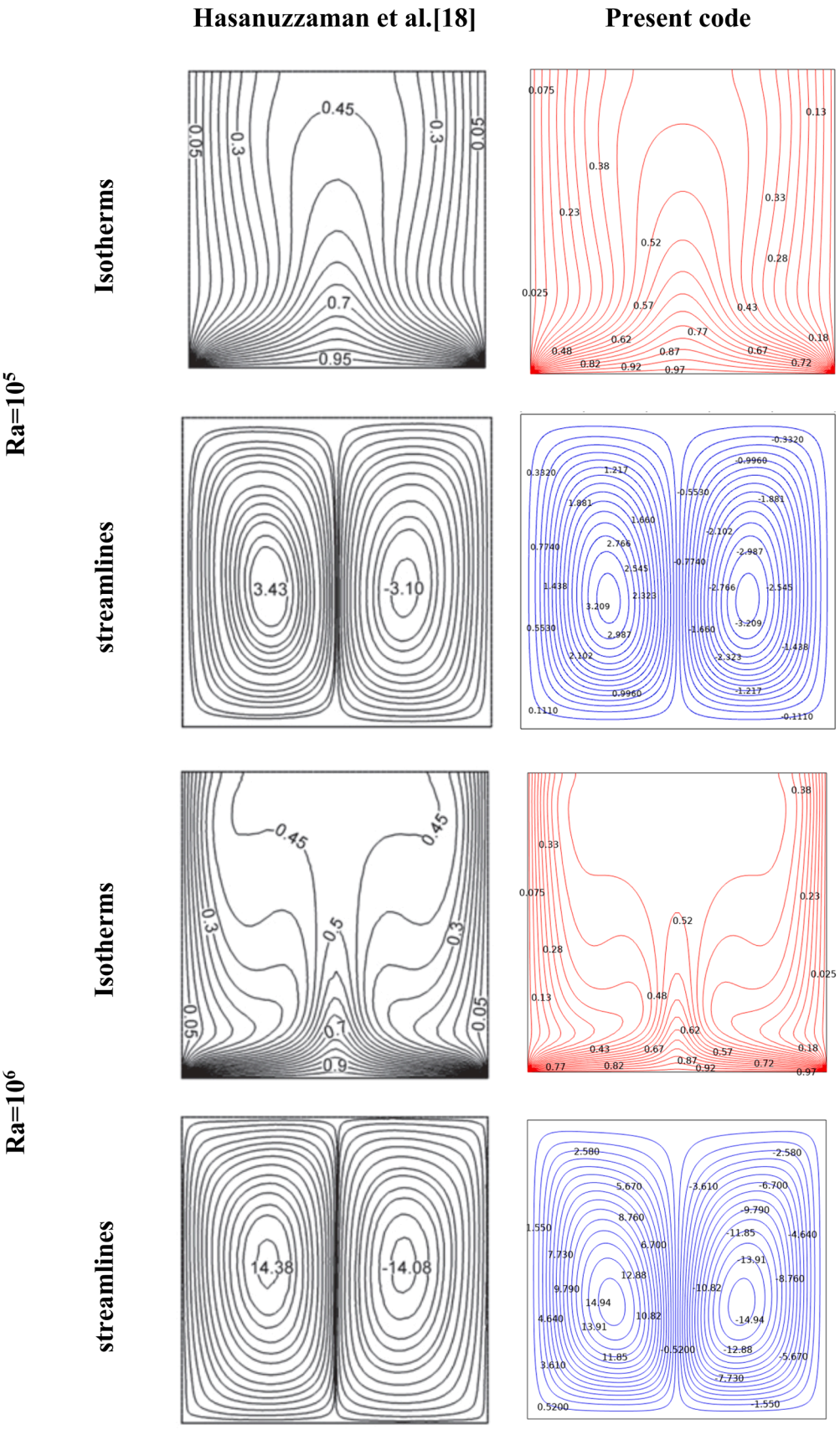

Fig. 4. Validation of the results between current study and study of [18].

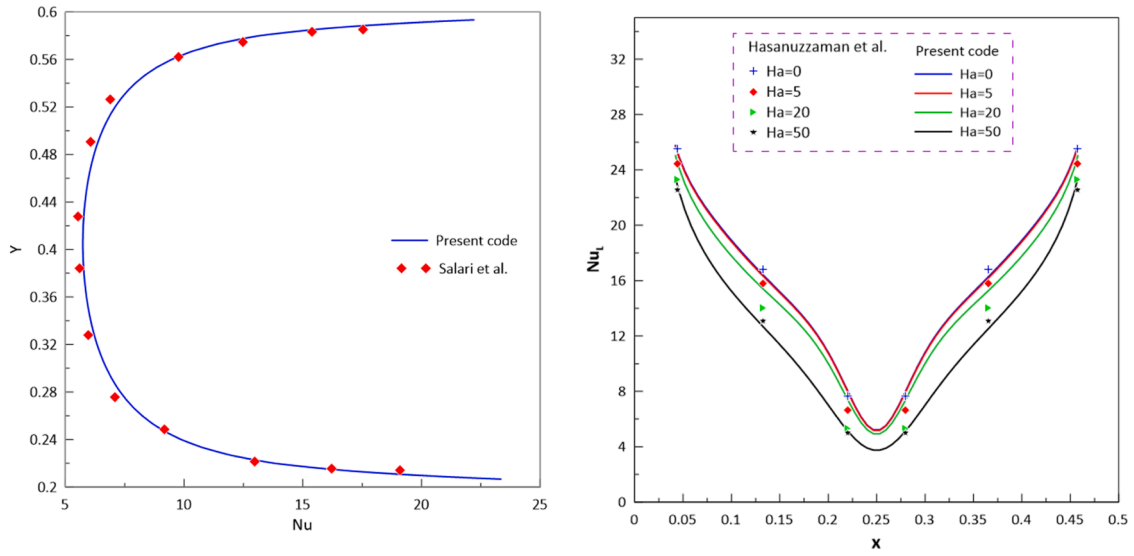

Fig. 5. Comparison in term of local Nusselt number of the current study and studies of [18,54].

3.1. Grid independence test

The grid used during the current study is a mixture of quads and triangular elements, as shown in Fig. 2. The quads elements cover the areas near the walls due to the formation of the boundary layer, while the rest of the domain will be triangular elements. Different schemes of discretization are performed to get the optimal one in terms of time and accuracy. Table 2 lists all the data related to the testing procedure, and the average Nusselt number is chosen as the main parameter that is checked persistently. Fourth Grid **G4** shows promising accuracy and saved time, and therefore it has been chosen to do all numerical analysis of different cases in the current study.

3.2. Verification of results

The reliability and accuracy of the numerical code used have been tested by comparing its results with those of other papers. The first validation is performed with the work of Salari et al. [54] comparing the isothermal lines and streamlines as shown in Fig. 3. The second one has been introduced with the work of Hasanuzzaman et al. [18] at different parameters, as shown in Fig. 4. Another validation in terms of the Nusselt number has been done for the abovementioned studies [18,54], as shown in Fig. 5. The local Nusselt number comparison demonstrates a maximum deviation of 1.9 % with Salari et al. [54] and 2.2 % with Hasanuzzaman et al. [18], confirming the high accuracy of our numerical code.

4. Results and discussion

The parameter ranges in this study were carefully selected to ensure both physical significance and practical applicability. The Rayleigh number range ($Ra = 10^3 - 10^6$) was chosen to capture the transition from conduction-dominated to convection-dominated heat transfer, covering most practical thermal management applications. The Hartmann number range ($Ha = 0 - 50$) spans from pure hydrodynamic flow to strong magnetic effects, reflecting achievable magnetic field strengths in industrial applications. The wave amplitude ($w_a = 0.01 - 0.15$) and wave number ($w_n = 0 - 6$) ranges were selected based on manufacturability constraints and practical heat exchanger designs, providing a spectrum from nearly flat walls to pronounced waviness. The magnetic field inclination angle range ($\gamma = 0° - 90°$) encompasses all practical field orientations, enabling comprehensive understanding of directional effects on flow and heat transfer. These ranges ensure that our results are both physically meaningful and directly applicable to real engineering systems, particularly in thermal management and heat exchanger applications.

Fig. 6 shows the effects of the Rayleigh number (Ra) on the isotherms and streamlines in the two-fluid layer. At low value of $Ra = 10^3$, the isotherms are nearly parallel to the horizontal walls, indicating that conduction is the dominant heat transfer mechanism. There's a slight distortion near the wavy walls, indicating weak convection effects. Isotherms significantly distort as Ra increases, particularly in the lower fluid layer. The center of the cavity shows vertical isotherms, indicating strong convection currents. The upper fluid layer (likely air) shows less distortion, suggesting weaker convection. At $Ra = 10^6$, isotherm distortion in the lower fluid layer is extreme, with almost vertical lines in the center. This indicates extreme convection currents in the nanofluid layer. The upper layer still shows some horizontal stratification, but with increased distortion. At Ra between 10^3 to 10^4, two weak circulation cells are visible in the lower fluid layer. The upper layer's circulation is very weak, almost negligible. At Ra between 10^4 to 10^6, very intense circulation cells in the lower fluid layer, with compact core regions. The upper layer exhibits stronger circulation patterns, though still weaker than the lower layer.

Fig. 7 depicts the effects of varying the wave amplitude (w_a) on the isotherms and streamlines in the two-fluid layer. The isotherms are nearly parallel to the horizontal walls, especially in the upper layer at $w_a = 0.01$. There's slight distortion in the lower layer, indicating weak convection. As w_a increases to 0.15, extreme distortion of isotherms, especially in the lower fluid layer. The wavy wall geometry has a significant impact on the temperature distribution, with pronounced hot and cold regions corresponding to the wall undulations. At low values of w_a, the streamlines are mostly symmetrical and aligned with the nearly straight walls. As w_a increases, very pronounced circulation cells in both layers are strongly influenced by the wavy geometry. The lower layer shows more compact and intense circulation patterns. The upper layer circulation extends further into the cavity. The lower fluid layer (likely the nanofluid) shows more sensitivity to changes in w_a compared to the upper layer (likely air). Increasing w_a leads to the formation of local hot and cold spots near the wavy walls, potentially enhancing heat transfer. As w_a increases, the circulation patterns become more complex and intense, indicating increased convective heat transfer.

Fig. 8 illustrates the effects of varying the number of waves (w_n) on the isotherms and streamlines in the two-fluid layer. At $w_n = 1$: The isotherms show a single large undulation corresponding to the single wave on each wall. There's significant distortion in the lower fluid layer,

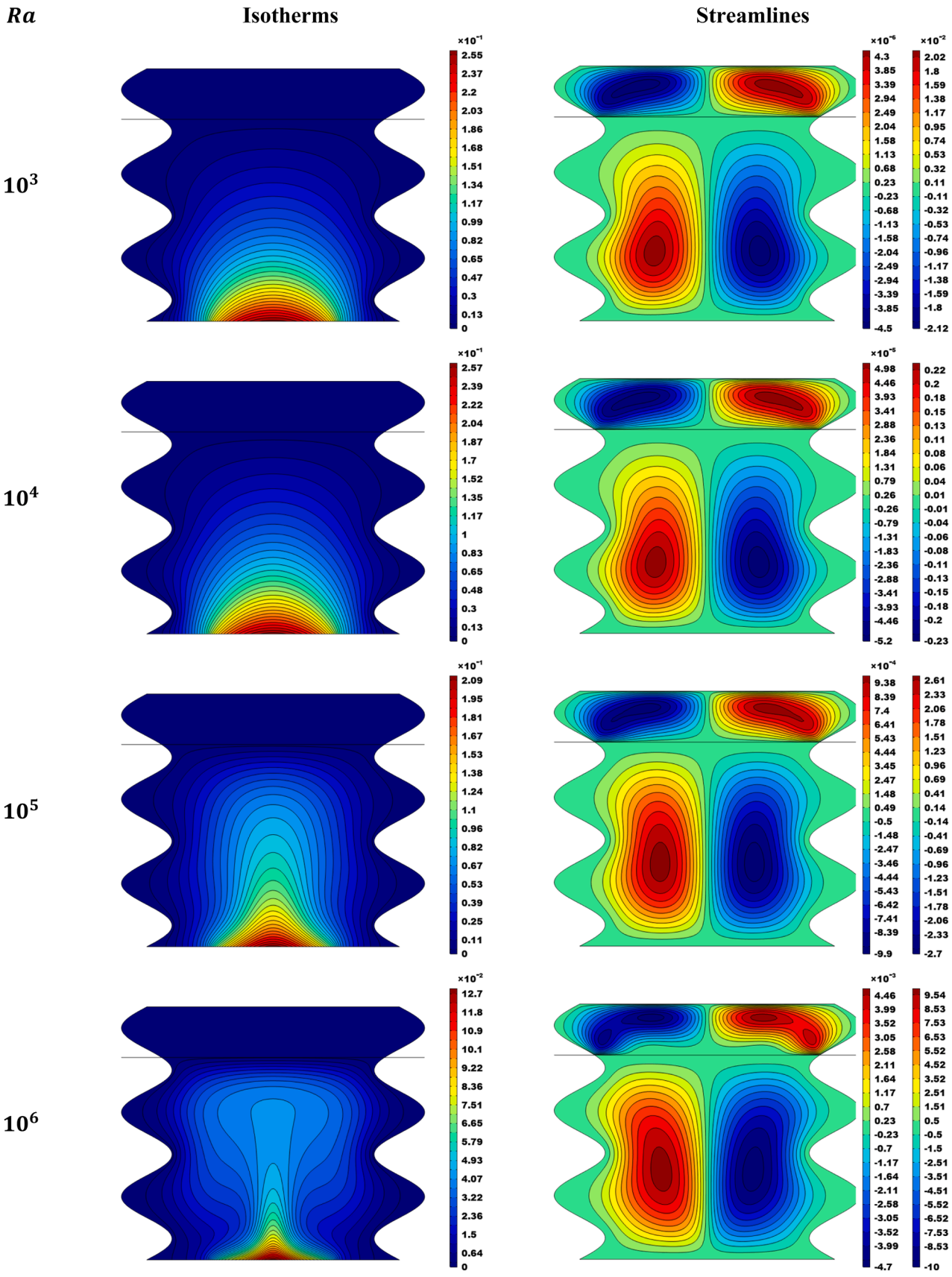

Fig. 6. The countors of θ and Ψ (left legend for air and right legend for nanofluid) for various *Ra* ($w_n = 3$, w_a =0.1, $Ha = 10$, φ = 0.02, γ = 90^o).

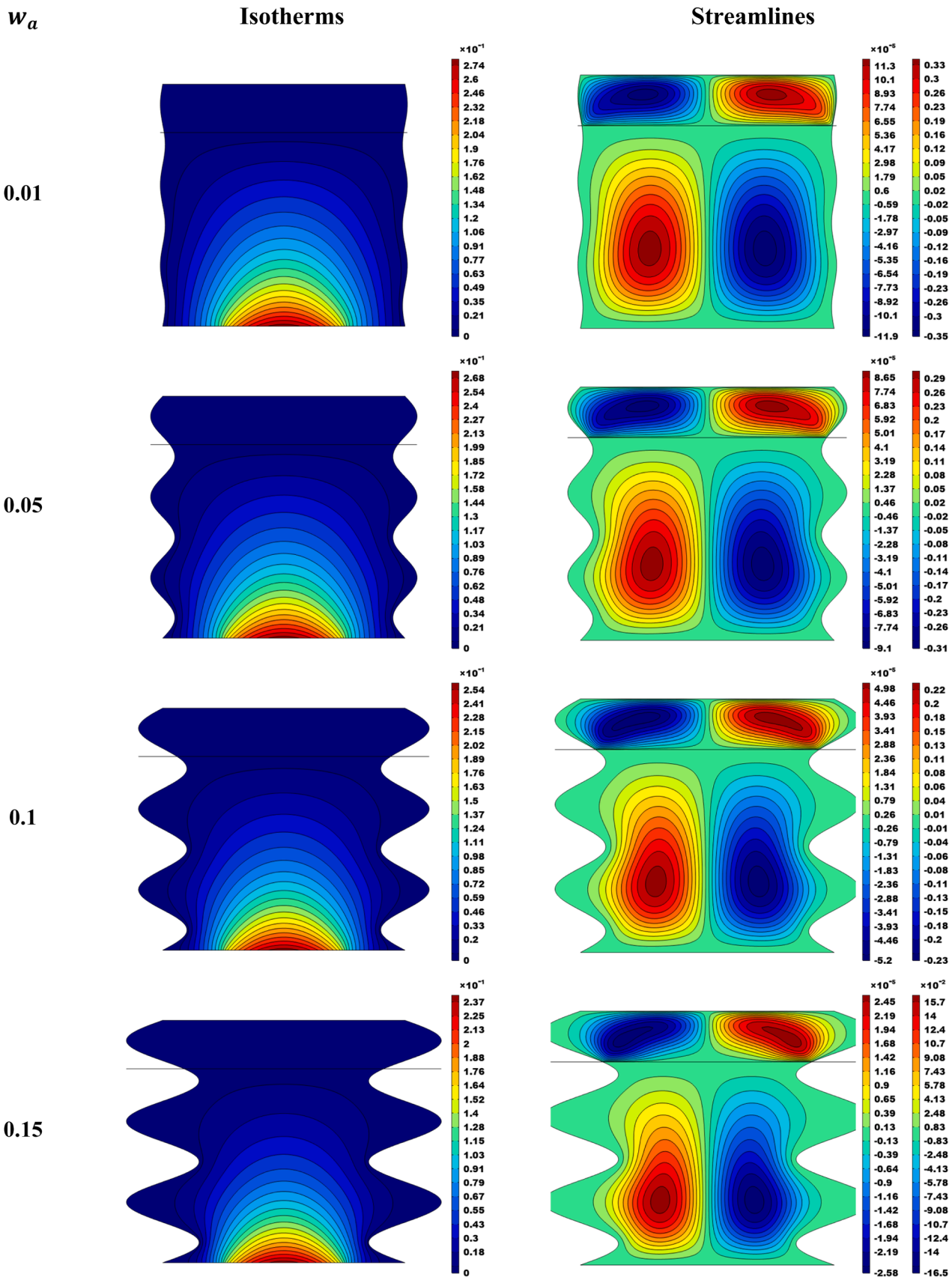

Fig. 7. The countors of θ and Ψ for various w_a ($Ra = 10^4$, $w_n = 3$, $Ha = 10$, $\varphi = 0.02$, $\gamma = 90^o$).

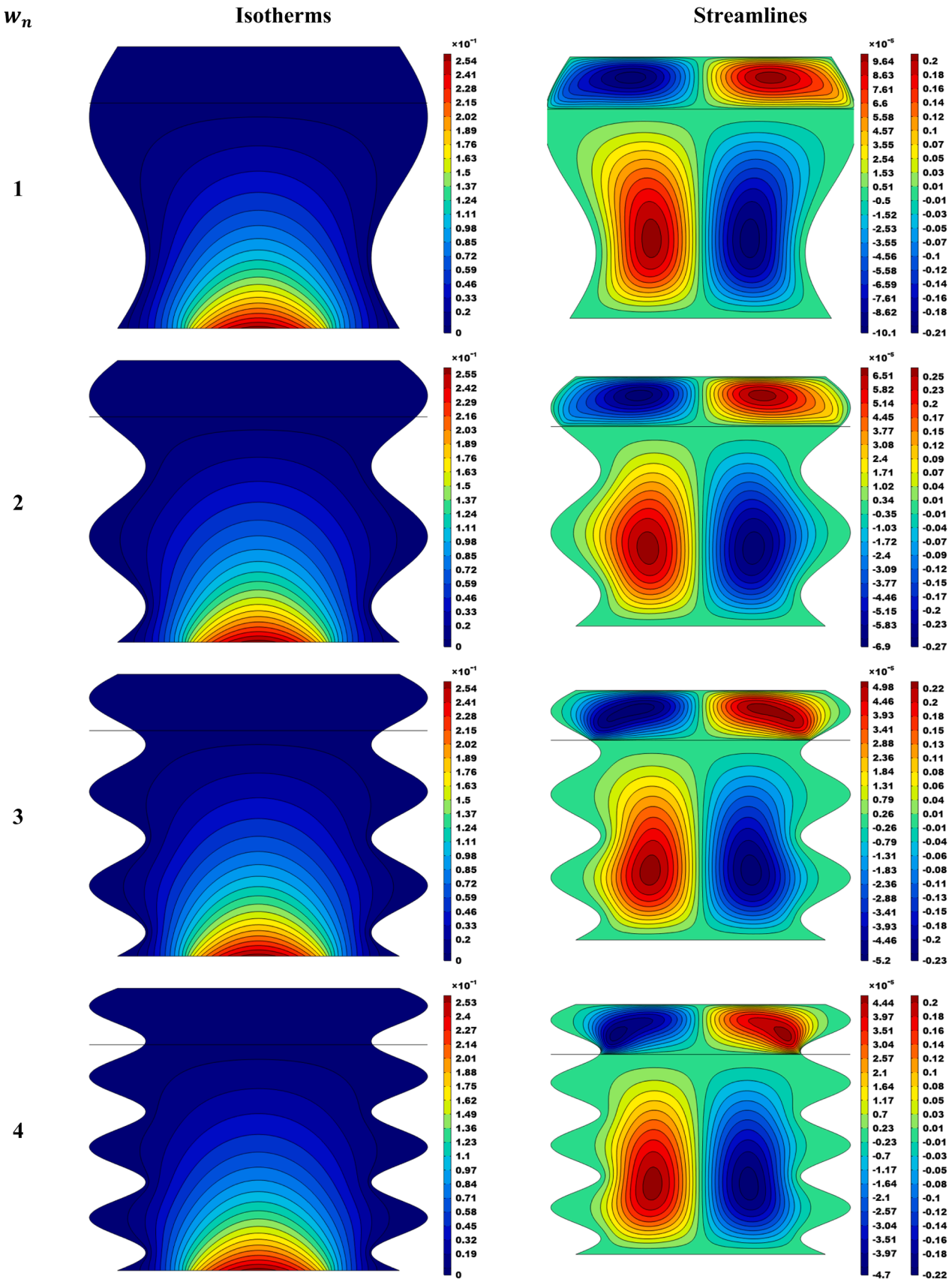

Fig. 8. The countors of θ and Ψ for various w_n ($Ra = 10^4$, w_a =0.1, $Ha = 10$, φ = 0.02, γ = 90^o).

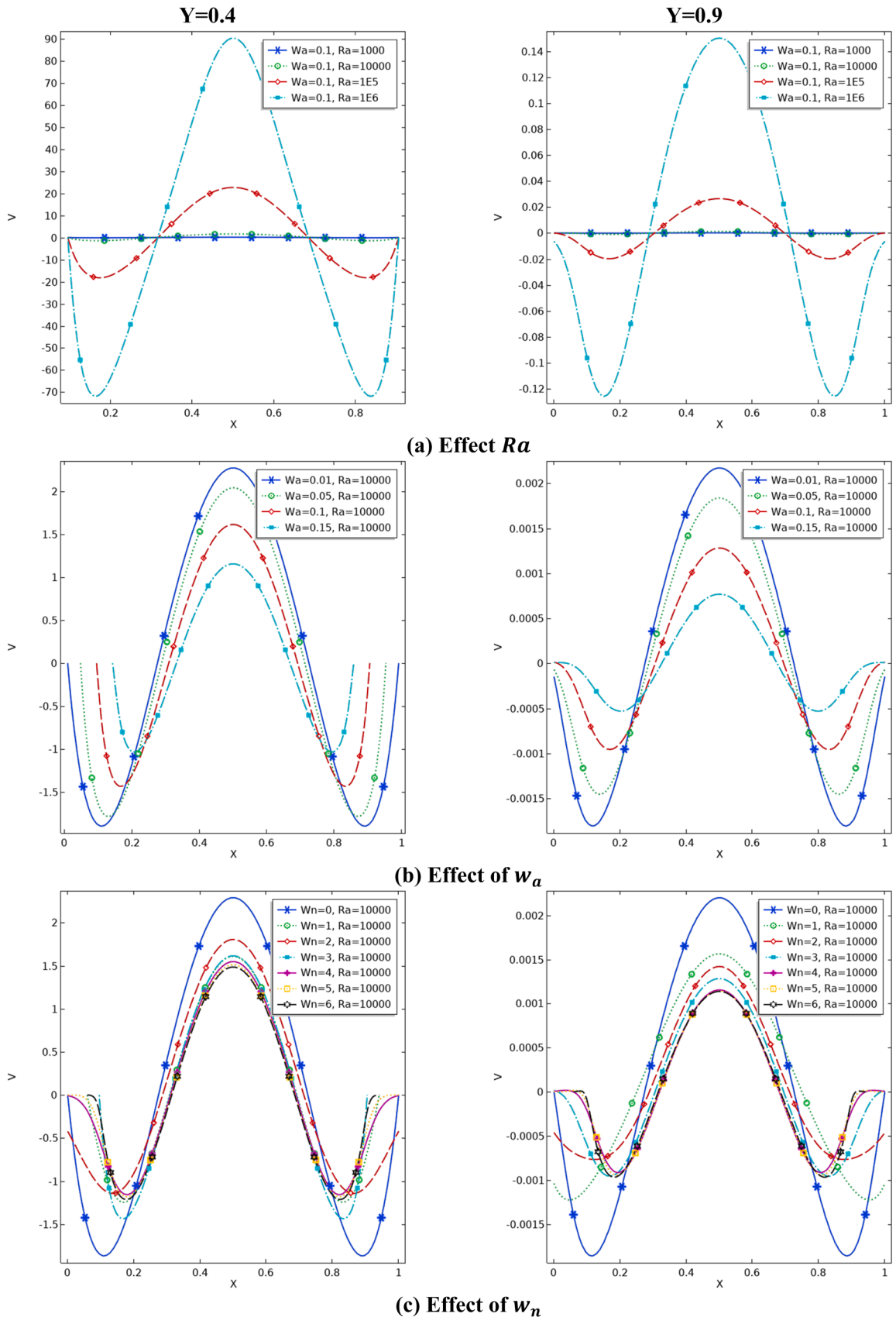

Fig. 9. Velocity profile at two different positions for various (a) *Ra*, (b) w_a, (c) w_n ($Ra = 10^4$, $w_a = 0.1$, $w_n = 3$, $Ha = 10$, $\varphi = 0.02$, $\gamma = 90^o$).

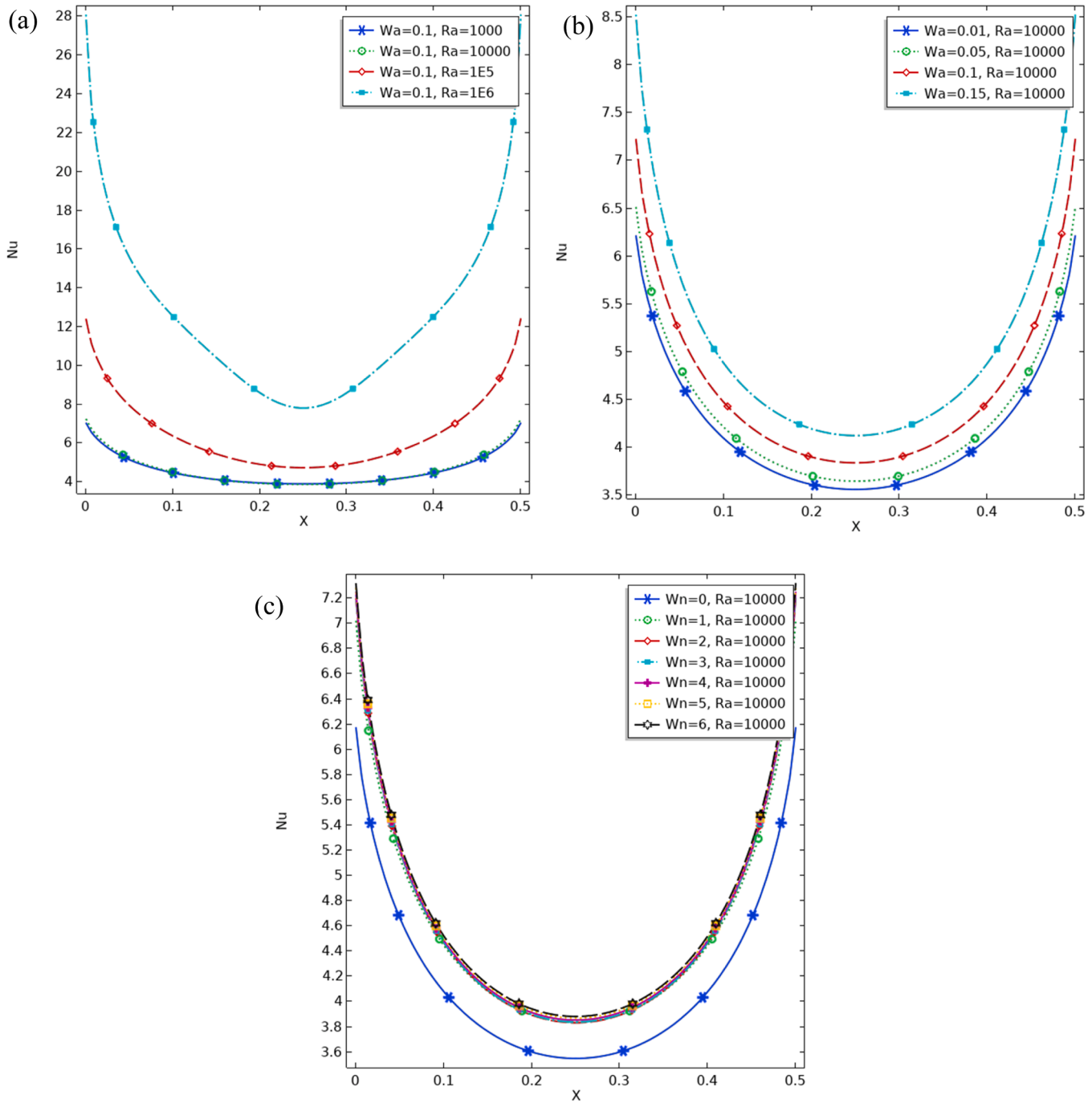

Fig. 10. Local Nusselt number varation for various (a) *Ra*, (b) w_a, (c) w_n.

indicating convection. The upper layer shows less distortion, suggesting weaker convection. This behavior is primarily due to the higher thermal conductivity and density of the lower fluid layer, resulting in stronger buoyancy-driven flows. As w_n increased to 4, the isotherms in the lower layer became highly distorted and complex. The upper layer shows increased distortion compared to lower w_n values. This enhanced distortion occurs because multiple waves create additional vortex generation points, leading to stronger secondary flows and improved fluid mixing. The lower layer now shows four distinct circulation regions, closely following the wave pattern. These circulation regions form due to the interaction between wall curvature and buoyancy forces, creating local pressure gradients that drive secondary flows. The upper layer circulation becomes more intricate, with multiple smaller vortices. This multiplication of vortices enhances the interfacial mixing between the two fluid layers, contributing to improved overall heat transfer efficiency through increased surface area for thermal exchange.

Fig. 9 presents the velocity profiles at two different vertical positions ($Y = 0.4$ and $Y = 0.9$) for various Rayleigh numbers (Ra) ranging from 10^3 to 10^6. This comparison allows us to analyze the effect of Ra on the fluid flow characteristics in both the lower and upper regions of the cavity. $Y = 0.4$ likely represents a position in the lower fluid layer (nanofluid), $Y = 0.9$ likely represents a position in the upper fluid layer (air). The distinct behavior at these positions reflects the fundamental differences in fluid properties and their response to buoyancy forces. As Ra increases from 10^3 to 10^6, the flow transitions from conduction-dominated to convection-dominated, particularly in the lower layer (Y

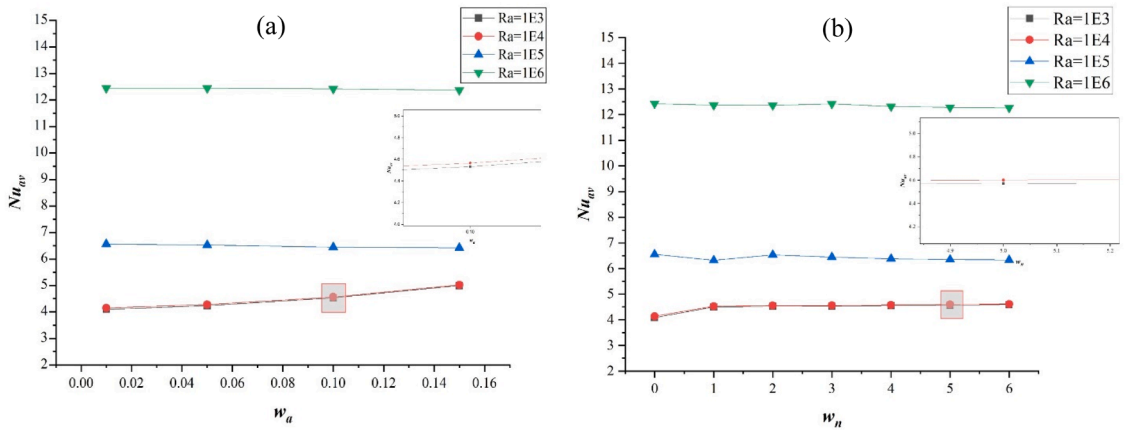

Fig. 11. Variation of the average Nusselt number with (a) w_a, (b) w_n, and Ra .($Ha = 10$, $\varphi = 0.02$, $\gamma = 90^o$).

$= 0.4$). This transition occurs due to the increasing dominance of buoyancy forces over viscous forces, characterized by the ratio $g\beta\Delta TL^3/\nu\alpha$. At $Ra = 10^3$, velocities are near-zero, indicating minimal convection. As Ra rises, velocities increase dramatically, reaching peaks of about 90 units at Ra=10^6 in the lower layer, compared to only 0.14 units in the upper layer ($Y = 0.9$). This difference is due to the lower layer's likely higher density and thermal conductivity, making it more responsive to buoyancy forces. The magnitude difference of approximately 640 times between layers demonstrates the strong influence of fluid properties on convection strength. The sinusoidal velocity profiles at higher Ra values indicate the formation of strong convection cells. These cells are driven by the coupling between thermal and momentum boundary layers, where the wall waviness induces periodic flow separation and reattachment. The upper layer shows similar but much weaker trends, suggesting less sensitivity to Ra changes. As w_a increases from 0.01 to 0.15, the maximum velocity in the lower layer ($Y = 0.4$) decreases from about 2.3 to 1.2 units, while in the upper layer ($Y = 0.9$), it drops from 0.0023 to 0.0008 units. This decrease is likely due to increased flow resistance from the more pronounced wavy walls. The lower layer shows significantly higher velocities, indicating stronger convection currents. The wavy walls (higher w_n) tend to disrupt these layers boundary, potentially enhancing heat transfer. For lower w_n values, the central region ($x = 0.4$ to 0.6) shows more uniform velocities, while higher wn creates more variability across the entire cavity width.

Fig. 10 demonstrates the local Nusselt number (Nu) variation along the heated bottom surface for different Rayleigh numbers (Ra), wave amplitudes (w_a), and wave numbers (w_n). Increasing Ra from 10^3 to 10^6 significantly enhances heat transfer, with peak Nu values rising from about 7 to 28. This is due to stronger buoyancy-driven convection at higher Ra, intensifying fluid circulation and thermal transport. This enhancement occurs through the development of thinner thermal boundary layers and stronger temperature gradients near the heated surface, where the ratio of convective to conductive heat transfer increases by approximately 300 %. Larger w_a (from 0.01 to 0.15) moderately increases Nu, with maximum values rising from about 5.5 to 7.5 at $Ra = 10^4$. Increased wall waveness promotes mixing and disrupts thermal boundary layers, enhancing heat transfer. The wavy geometry creates periodic flow separation and reattachment points, generating secondary flows that enhance local mixing. This mechanism is particularly effective near the cavity edges where the interaction between wall curvature and buoyancy forces is strongest. Higher w_n (0 to 6) slightly improves heat transfer, particularly near the cavity edges. The effect is less pronounced than w_a, with Nu increasing from about 6 to 7 at the edges for $Ra = 10^4$. This moderate enhancement is attributed to the formation of multiple smaller recirculation zones that increase local mixing but also create competing effects between adjacent waves, potentially limiting the overall heat transfer improvement.

Fig. 11a demonstrates the combined effects of wave amplitude (w_a) and Rayleigh number (Ra) on the average Nusselt number (Nu_{av}). As Ra increases from 10^3 to 10^6, Nu_{av} significantly increases, indicating enhanced heat transfer. This is due to stronger buoyancy-driven convection at higher Ra values. This enhancement occurs through two primary mechanisms: first, the increased temperature gradient creates stronger density differences, leading to more vigorous fluid motion; second, the resulting stronger convection cells reduce the thermal boundary layer thickness, improving heat transfer efficiency. For instance, at $w_a = 0.01$, Nu_{av} rises from 4.1006 to 12.442 as Ra increases from 10^3 to 10^6. This represents a 203 % improvement in heat transfer, demonstrating the dominance of convective transport over conductive transport at higher Ra values. At lower Ra (10^3 and 10^4), increasing w_a from 0.01 to 0.15 moderately enhances Nu_{av}. For $Ra = 10^3$, Nu_{av} increases from 4.1006 to 4.9984. This enhancement occurs because at low Ra, the wall waviness effectively disrupts the thick thermal boundary layer, creating secondary flows that improve mixing without significantly increasing flow resistance. At higher Ra (10^5 and 10^6), increasing w_a slightly decreases Nu_{av}. For $Ra = 10^6$, Nu_{av} decreases from 12.442 to 12.369. This slight decrease can be attributed to the competing effects between enhanced mixing from wall waviness and increased flow resistance, where at high Ra, the additional friction losses from larger wave amplitudes slightly outweigh the benefits of improved mixing.

Fig. 11b illustrates the combined effects of wave number (w_n) and Rayleigh number (Ra) on the average Nusselt number (Nu_{av}). As Ra increases from 10^3 to 10^6, Nu_{av} significantly increases across all w_n values, indicating enhanced heat transfer due to stronger buoyancy-driven convection. This enhancement is characterized by the transition from a conduction-dominated regime to a convection-dominated regime, where the thermal boundary layer thickness decreases proportionally to $Ra^{-\frac{1}{4}}$. For example, at $w_n = 0$, Nu_{av} rises from 4.0848 to 12.426 as Ra increases from 10^3 to 10^6. For lower Ra (10^3 and 10^4), increasing w_n generally leads to a moderate increase in Nu_{av}. At $Ra = 10^3$, Nu_{av} increases from 4.0848 ($w_n = 0$) to 4.5897 ($w_n = 6$). This improvement occurs because multiple waves create a series of sequential mixing zones, where each wave crest acts as a local flow perturbation point, enhancing fluid mixing in the conduction-dominated regime. For higher Ra (10^5 and 10^6), the effect of w_n on Nu_{av} is less consistent and shows a slight decreasing trend for very high Ra. At $Ra = 10^6$, Nu_{av} decreases from 12.426 ($w_n = 0$) to 12.267 ($w_n = 6$). This behavior can be attributed to the interference between adjacent wave-induced vortices, where at high Ra, the closely spaced waves create competing flow structures that partially cancel each other's mixing effects. The impact of w_n on heat transfer is more pronounced at lower Ra values, suggesting that optimizing wall waviness is more critical in regimes where conduction plays a significant role. This highlights the importance of geometric optimization in different flow regimes, where wall waviness can

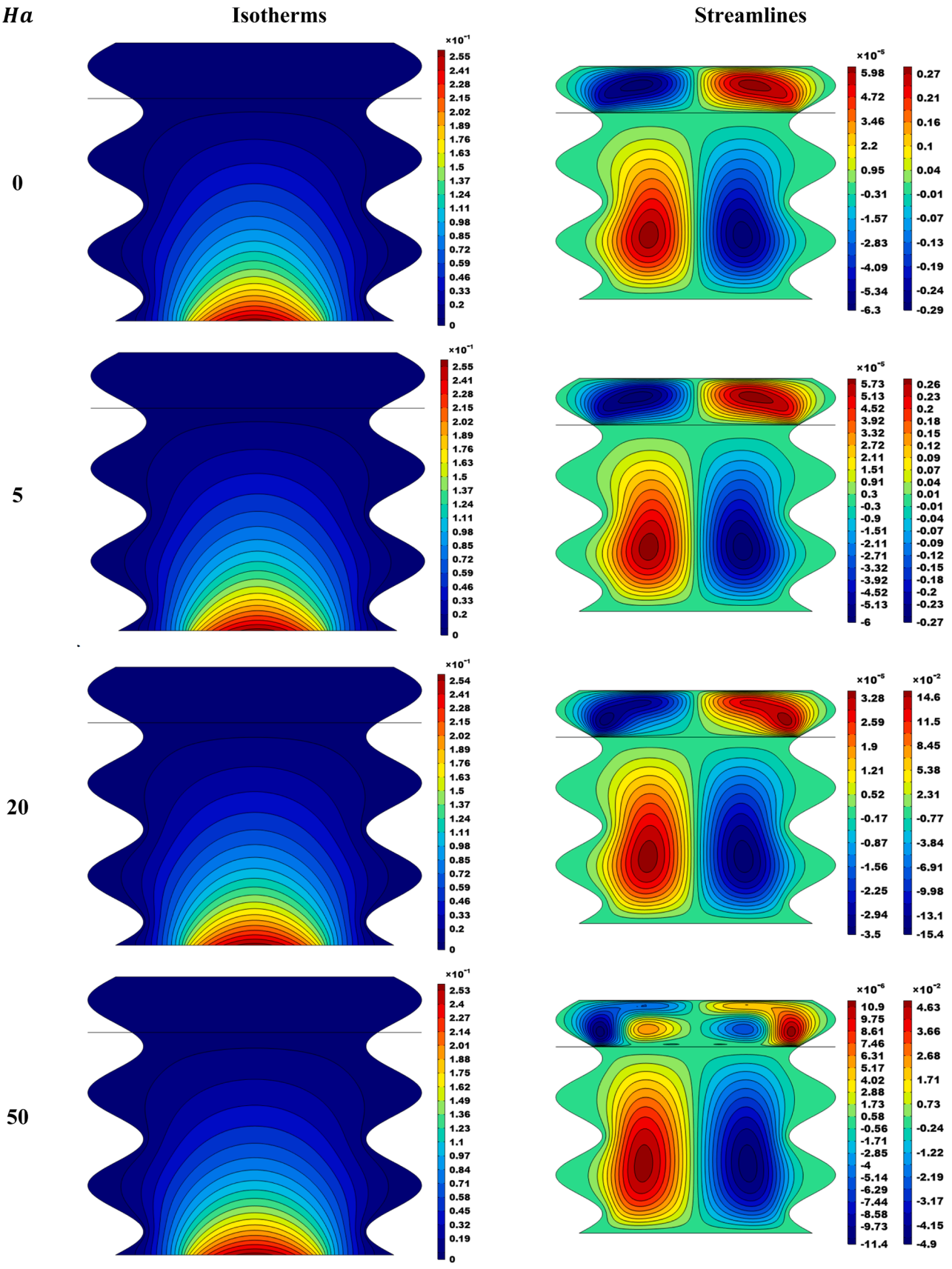

Fig. 12. The countors of θ and Ψ for various *Ha* ($w_n = 3$, w_a =0.1, $Ra = 10^4$, φ = 0.02, γ = 90°).

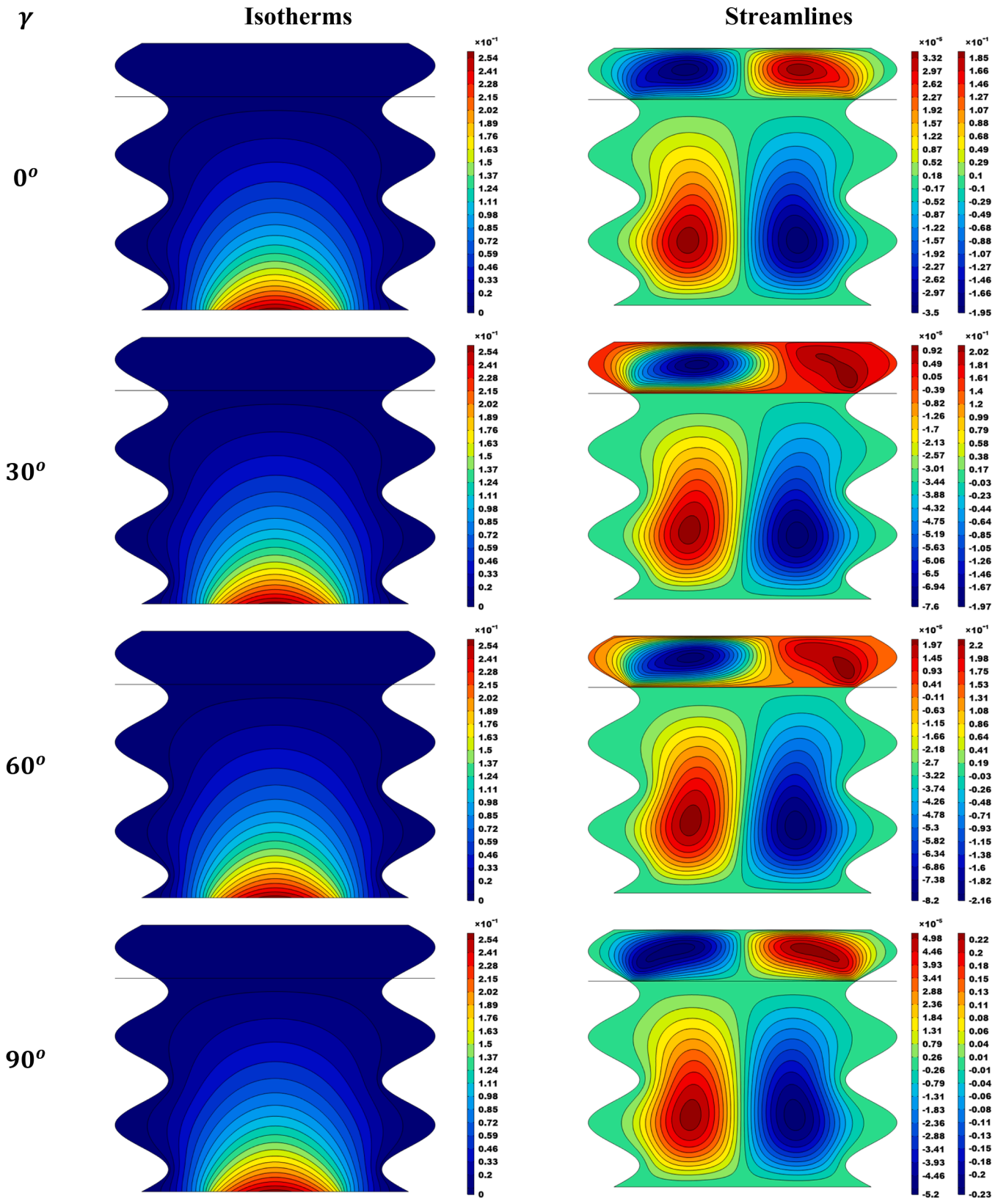

Fig. 13. The countors of θ and Ψ for various γ ($w_n = 3$, w_a =0.1, $Ra = 10^6$, φ = 0.02, $Ha = 10$).

effectively compensate for weaker natural convection at lower Ra.

Fig. 12 displays the impact of increasing Hartmann number (*Ha*) on both temperature distribution (isotherms) and fluid flow patterns (streamlines) in a wavy cavity with two immiscible fluids under an applied magnetic field. The temperature contours become more horizontal and evenly spaced, especially in the upper fluid layer. This indicates a shift from convection-dominated to conduction-dominated heat transfer as the magnetic field strengthens. The thermal

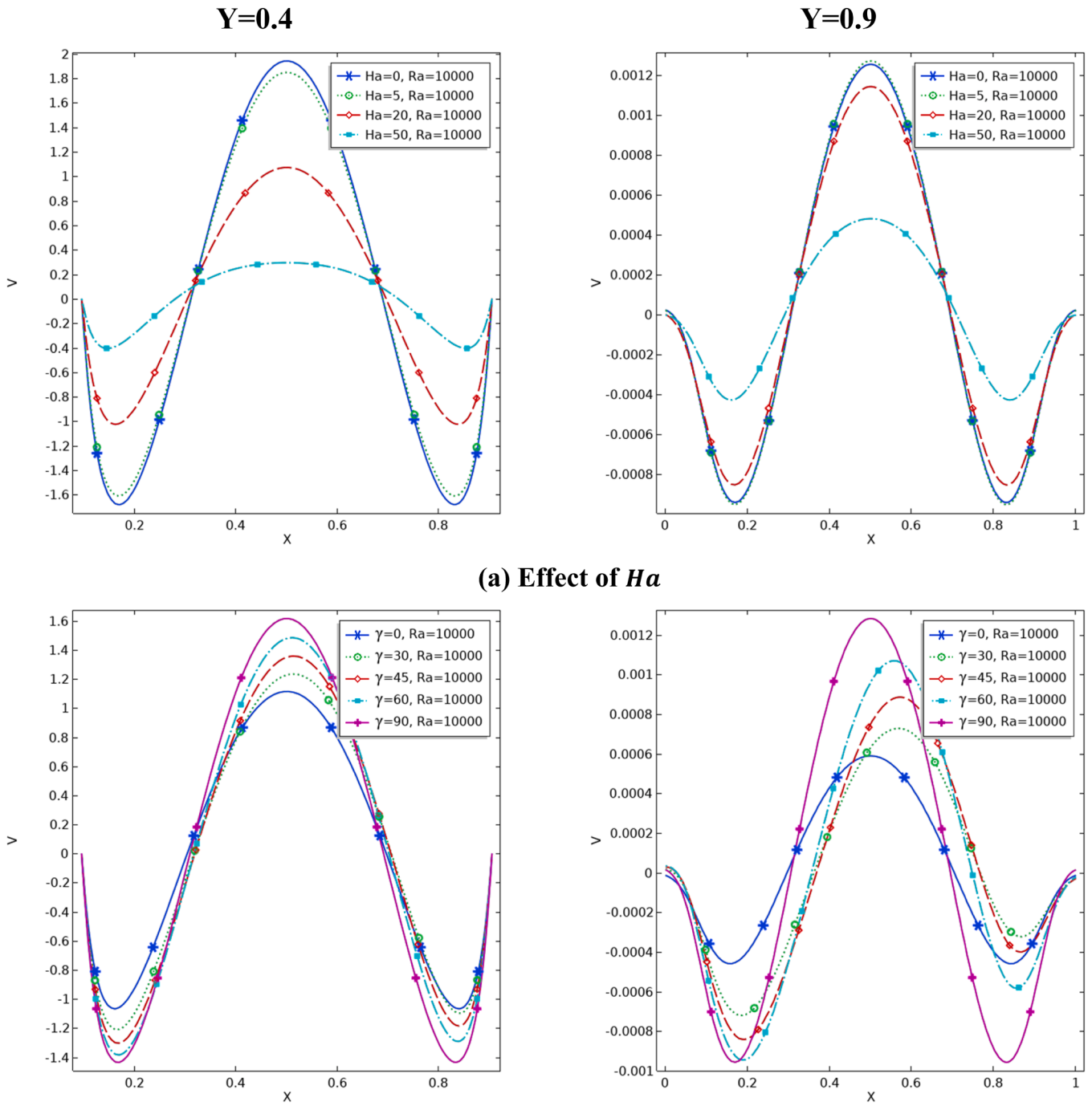

Fig. 14. Velocity profile at two different positions for various (a) *Ha*, (b) γ, ($Ra = 10^4$, $w_a = 0.1$, $w_n = 3$, $Ha = 10$, φ = 0.02, γ = 90°).

stratification in the upper layer becomes more pronounced at higher *Ha* values. The flow pattern transitions from two large, symmetric convection cells at $Ha = 0$ to smaller, compressed cells concentrated near the cavity walls at $Ha = 50$. The core flow weakens significantly, as evidenced by the reduced density of streamlines in the center. This is due to the magnetic field's dampening effect on fluid motion, particularly in the electrically conducting lower layer.

Fig. 13 explains the effect of varying the magnetic field inclination angle (γ) on temperature distribution (isotherms) and fluid flow patterns (streamlines) in a wavy cavity with two immiscible fluids. As γ increases from 0° to 90°: The temperature contours remain relatively consistent across all angles, with slight variations in the upper fluid layer. This suggests that the inclination angle has a minor impact on overall heat transfer. The flow pattern shows more significant changes. At $\gamma = 0°$, two symmetrical convection cells are present. As γ increases, the right cell becomes dominant, growing in size and intensity (indicated by denser streamlines), while the left cell weakens and shrinks.

Fig. 14 portrays the velocity profiles at two vertical positions ($Y = 0.4$ and $Y = 0.9$) for varying Hartmann numbers (*Ha*) and magnetic field inclination angles (γ). As *Ha* increases from 0 to 50, the velocity magnitude decreases significantly, especially at $Y = 0.4$. At $Y = 0.4$, the peak velocity drops from about 1.8 ($Ha = 0$) to 0.2 ($Ha = 50$). The

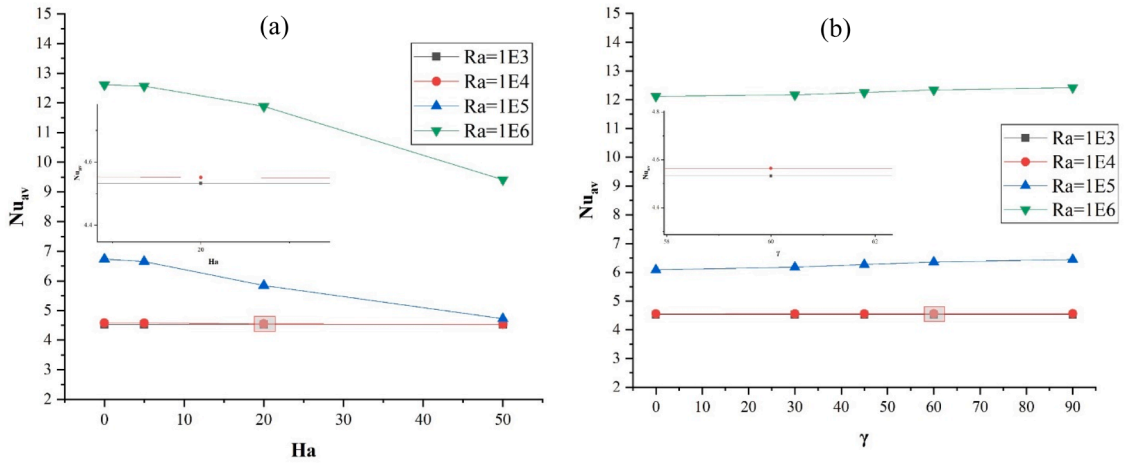

Fig. 15. The average Nusselt number with (a) *Ha*, (b) γ, and *Ra* .($w_a = 0.1$, $w_n = 3$, φ = 0.02).

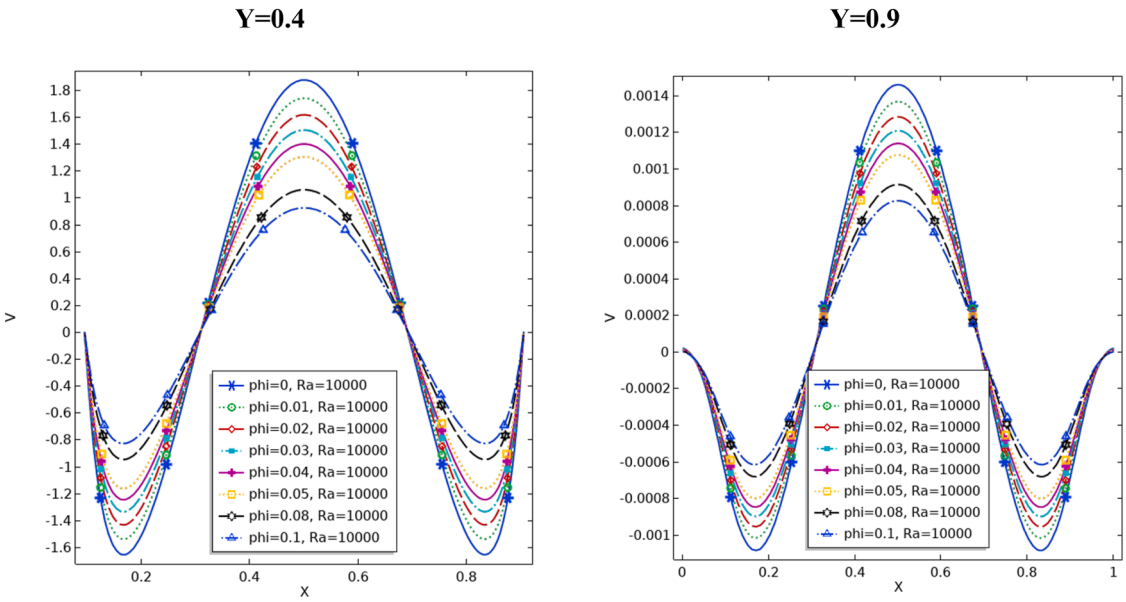

Fig. 16. Velocity profile at two different positions for various nano concentration (φ), ($Ra = 10^4$, $w_a = 0.1$, $w_n = 3$, $Ha = 10$, $\gamma = 90^o$).

velocity profile flattens with increasing Ha, indicating suppression of fluid motion. The effect is less pronounced at $Y = 0.9$, suggesting stronger magnetic damping in the lower fluid layer. Changing γ from 0° to 90° alters the velocity profile shape and magnitude. At $Y = 0.4$, the peak velocity increases from about 1.2 ($\gamma = 0°$) to 1.5 ($\gamma = 90°$). The profile becomes more asymmetric at intermediate angles ($30° - 60°$). At $Y = 0.9$, the effect is more pronounced, with significant changes in profile shape and magnitude. These results demonstrate that increasing the magnetic field strength (*Ha*) suppresses fluid motion, particularly in the lower, more electrically conductive layer. The magnetic field orientation (γ) influences flow asymmetry and intensity, with vertical orientation (90°) generally allowing for stronger fluid motion. The significant velocity difference between $Y = 0.4$ and $Y = 0.9$ highlights the distinct flow behaviors in the two fluid layers, likely due to differences in electrical conductivity and proximity to the heated bottom surface.

Fig. (15a) demonstrates the combined effects of Hartmann number (Ha) and Rayleigh number (Ra) on the average Nusselt number (Nu_{av}) for fixed wave amplitude, magnetic field angle, wave number, and nanoparticle volume fraction. At lower Ra (10^3 and 10^4), increasing Ha has minimal effect on Nu_{av}. For $Ra = 10^3$, Nu_{av} only decreases slightly from 4.5326 (Ha = 0) to 4.5311 (Ha = 50). This minimal impact occurs because at low Ra, heat transfer is primarily conductive, and the Lorentz force has little influence on the already weak fluid motion. At higher Ra (10^5 and 10^6), increasing Ha significantly reduces Nu_{av}. For $Ra = 10^6$, Nu_{av} decreases from 12.613 (Ha = 0) to 9.4118 (Ha = 50). This substantial reduction (approximately 25.4 %) results from the magnetic field's induced Lorentz force, which acts perpendicular to both the fluid motion and the magnetic field direction. The force creates additional flow resistance that suppresses convective currents and thickens the thermal boundary layer. The suppressive effect of Ha on heat transfer becomes more pronounced at higher Ra values. This suggests that the magnetic field's damping effect on fluid motion is more significant when convection is stronger. This behavior can be explained by the quadratic relationship between the Lorentz force and fluid velocity, where stronger convective flows at higher Ra experience proportionally greater magnetic damping, leading to a more pronounced reduction in heat transfer efficiency.

Fig. 15b illustrates the combined effects of magnetic field inclination angle (γ) and Rayleigh number (Ra) on the average Nusselt number (Nu_{av}). At lower Ra (10^3 and 10^4), changing γ has minimal effect on Nu_{av}. For $Ra = 10^3$, Nu_{av} only increases slightly from 4.5321 (γ=0°) to 4.5323 (γ=90°). This minimal sensitivity at low Ra occurs because the

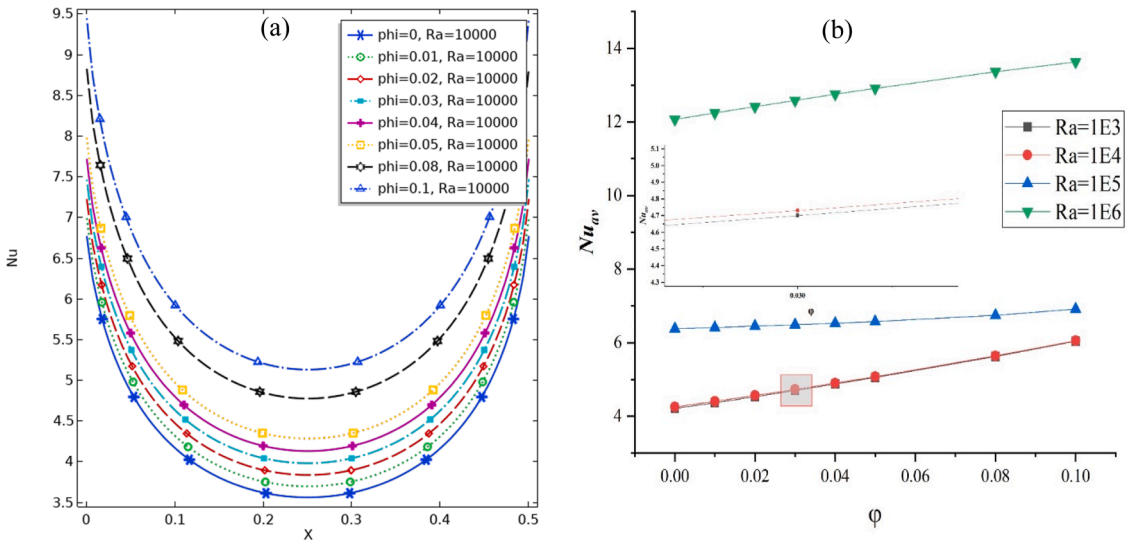

Fig. 17. Effect of nano concentration (φ) on (a) local Nusselt number, (b) averag Nusselt number ($w_a = 0.1$, $w_n = 3$, $Ha = 10$, $\gamma = 90^o$).

conduction-dominated heat transfer is largely independent of fluid motion, making the magnetic field orientation less influential. At higher Ra (10^5 and 10^6), increasing γ moderately enhances Nu_{av}. For $Ra = 10^6$, Nu_{av} increases from 12.118 (γ = 0°) to 12.417 (γ = 90°). This enhancement occurs because the vertical magnetic field orientation (γ = 90°) allows for stronger vertical convection currents while still maintaining some flow control. The Lorentz force components vary with sin (γ), resulting in optimal alignment with the primary buoyancy-driven flow at γ = 90° The positive effect of increasing γ on heat transfer becomes more pronounced at higher Ra values, suggesting that the magnetic field orientation plays a more significant role when convection is stronger. This is due to the increased interaction between the magnetic field and the stronger fluid velocities at higher Ra, where the orientation-dependent Lorentz force can more effectively modulate the flow patterns. A vertical magnetic field (γ = 90°) consistently yields the highest Nu_{av}, especially at higher Ra values, indicating it's the most favorable orientation for heat transfer enhancement. This orientation minimizes the suppression of vertical convective flows while maintaining sufficient horizontal flow control to enhance mixing.

Fig. 16 shows the velocity profiles at two vertical positions ($Y = 0.4$ and $Y = 0.9$) for varying nanoparticle concentrations (φ) in a wavy cavity with an applied magnetic field. As φ increases from 0 to 0.1, the velocity magnitude generally decreases at both Y positions. At $Y = 0.4$, the peak velocity drops from about 1.9 (φ = 0) to 0.9 (φ = 0.1), a reduction of approximately 53 %. The effect is similar but less pronounced at $Y = 0.9$, with peak velocities decreasing from about 0.0014 to 0.0008. The overall profile shape remains similar across all φ values, maintaining a symmetrical pattern with positive velocities in the center and negative velocities near the walls. The profiles become slightly flatter with increasing φ, especially at $Y = 0.4$. Velocities at $Y = 0.4$ are about 1000 times larger than at $Y = 0.9$, indicating stronger fluid motion in the lower layer. The decrease in velocity with increasing nanoparticle concentration is likely due to the increased viscosity of the nanofluid. Higher viscosity leads to greater resistance to fluid motion, resulting in lower velocities. The effect is more pronounced in the lower layer ($Y = 0.4$) where the nanofluid is present, compared to the upper layer ($Y = 0.9$) which likely contains the base fluid.

Fig. 17 shows the effect of nanoparticle concentration (φ) on heat transfer performance, represented by local and average Nusselt numbers, for various Rayleigh numbers (*Ra*). *Nu* values are highest near the hot surface edges ($X = 0$ and $X = 0.5$) and lowest at the center (**see** Fig 17a). Increasing φ from 0 to 0.1 generally increases *Nu* across the cavity width. The effect is most pronounced near the edges, with *Nu* rising from about 7 to 9 at $x = 0$ for $Ra = 10^4$. Nu_{av} increases with φ for all *Ra* values, indicating enhanced overall heat transfer. The effect is more significant at higher *Ra*: At $Ra = 10^3$, Nu_{av} increases marginally from about 4.3 to 4.6 as φ rises from 0 to 0.1. At $Ra = 10^6$, Nu_{av} increases substantially from about 12 to 13.8 over the same φ range. Higher *Ra* values result in larger Nu_{av} for all φ concentrations. The slope of Nu_{av} vs. φ becomes steeper as *Ra* increases, showing a stronger nanoparticle effect at higher *Ra*. The enhancement in heat transfer with increasing nanoparticle concentration can be attributed to: (a) Increased thermal conductivity of the nanofluid, (b) Enhanced thermal dispersion due to nanoparticle motion, (c) Potential changes in fluid properties affecting convection. The more pronounced effect at higher *Ra* suggests that nanoparticles are particularly effective in enhancing heat transfer when convection is stronger. The U-shaped local *Nu* profile indicates that heat transfer is most intense near the cavity walls, where thermal gradients are steepest. These results demonstrate that adding nanoparticles can significantly improve heat transfer performance, especially in high-Ra systems, with up to 15 % increase in Nu_{av}observed for $Ra = 10^6$ as φ increases from 0 to 0.1.

The present cavity configuration offers several significant advantages for heat transfer applications. The wavy wall geometry enhances mixing and increases heat transfer surface area, while the inclined magnetic field provides non-intrusive flow control. The dual-layer immiscible fluid system, combining nanofluid and air layers, offers flexible thermal management through the combination of different fluid properties. Additionally, the adjustable wave parameters allow geometric optimization for specific applications.

However, the configuration also presents certain limitations that should be considered. These include manufacturing complexity of the wavy walls, potential increased flow resistance at higher Rayleigh numbers, and the need for external magnetic field equipment. The two-fluid system also requires careful management of interface stability and may need more frequent maintenance to preserve optimal performance characteristics.

The present study has direct applications in thermal desalination systems, where the two-layer configuration mirrors the practical setup of membrane distillation units. In these systems, the heated lower layer (saline water with nanoparticles) and cooled upper layer (freshwater) create the necessary temperature gradient for distillation. The wavy walls enhance mixing and heat transfer, while the magnetic field provides non-intrusive flow control - crucial features for optimizing desalination efficiency. Our studied parameters ($Ra = 10^3$-10^6, Ha=0–50) align with typical operating conditions in small to medium-scale

desalination units. For example, commercial membrane distillation systems operate with temperature differences creating Rayleigh numbers in the range of $10^4 - 10^6$, making our findings directly applicable to their design optimization.

5. Conclusions

In this study, MHD free convection of two immiscible fluids in waved cavity was carried out. The numerical results for different values of selected parameters are discussed based on its technological significance. The major findings based on the obtained results are summarized as follows:

1. Heat transfer enhancement is strongly dependent on Rayleigh number, with Nu_{av} increasing by 203 % (from 4.1006 to 12.442) as Ra rises from 10^3 to 10^6. Wall waviness effects are more pronounced at lower Ra, showing a 21.8 % increase in $Nu_{av}$with maximum wave amplitude.
2. Wall waviness effects are more pronounced at lower *Ra*. Increasing wave amplitude (w_a) from 0.01 to 0.15 enhances Nu_{av} by 21.8 % (from 4.1006 to 4.9984) at $Ra = 10^3$. Similarly, increasing wave number (w_n) from 0 to 6 improves Nu_{av} by 12.4 % (from 4.0848 to 4.5897) at $Ra = 10^3$.
3. Magnetic field strength significantly affects heat transfer at higher Ra, with Nu_{av} decreasing by 25.4 % at Ra=10^6 as Ha increases from 0 to 50. The vertical magnetic field orientation ($\gamma = 90^\circ$) provides optimal heat transfer conditions.
4. Magnetic field inclination angle (γ) moderately enhances heat transfer at higher *Ra*, with a 2.5 % increase in Nu_{av} (from 12.118 to 12.417) as γ changes from 0° to 90° at $Ra = 10^6$.
5. Nanoparticle concentration (φ) enhances overall heat transfer, especially at higher *Ra*. For $Ra = 10^6$, Nu_{av}increases by 15 % (from about 12 to 13.8) as φ rises from 0 to 0.1.
6. Velocity profiles show that increasing *Ha* from 0 to 50 reduces peak velocity by about 89 % (from 1.8 to 0.2) at $Y = 0.4$, indicating strong magnetic damping of fluid motion.
7. Nanoparticle addition suppresses fluid motion, with peak velocity at $Y = 0.4$ decreasing by 53 % (from 1.9 to 0.9) as φ increases from 0 to 0.1.
8. Local Nusselt number distributions show enhanced heat transfer near cavity edges, with values increasing from about 7 to 9 at the edges as φ increases from 0 to 0.1 for $Ra = 10^4$.

Based on our findings, we suggest several key areas for future research. Lab tests could verify our numerical predictions and reveal practical challenges in maintaining fluid interfaces and component durability. New approaches to enhance heat transfer could include investigating hybrid nanoparticles, alternative wall geometries, and time-dependent effects. The system could be adapted for specific applications such as solar thermal systems, electronic cooling units, and desalination plants. Advanced control strategies might explore pulsed magnetic fields, adaptive wall geometries, and automated system optimization. These research directions could advance our understanding of immiscible fluid systems and lead to improved practical applications in thermal management.

CRediT authorship contribution statement

Mohamed F. Al-Dawody: Supervision, Methodology, Formal analysis, Conceptualization. **Ahmed M. Hassan:** Validation, Software, Methodology. **Nasser H. Hamza:** Writing – original draft, Visualization, Resources, Formal analysis, Conceptualization. **Maathe A. Theeb:** Visualization, Investigation. **Mohammad Ghalambaz:** Writing – review & editing, Methodology. **Mikhail Sheremet:** Writing – review & editing, Project administration, Conceptualization.

Declaration of competing interest

The authors declare that they have no known competing financial interests or personal relationships that could have appeared to influence the work reported in this paper.

Acknowledgement

This research of Mikhail Sheremet and Mohammad Ghalambaz was supported by the Tomsk State University Development Programme (Priority-2030).

Data availability

Data will be made available on request.

References

[1] M.A. Alomari, et al., Convection flow of NE-phase change material-water mixture in evacuated tube solar collector manifold: numerical analysis of MHD double-diffusive convection and exothermic reaction, Int. Commun. Heat Mass Transf. 159 (2024) 108194.
[2] Hameed, R.H., et al., CFD analysis of mixed convection and entropy generation in vented curved cavity under the radiation effects, The European Physical Journal Plus. 2024. 139(8): p. 756.
[3] H.M. Al-Ali, N.H. Hamza, Numerical and experimental study of the influence of extended surfaces in rectangular channel subjected to constant heat flux, Experim. Heat Transf. 37 (6) (2024) 609–627.
[4] A.M. Hassan, et al., Active cooling of hot integrated circuits using a rotating cylinder and NEPCM-water mixture: numerical analysis of the impact of phase change and Magnetohydrodynamics on double-diffusive mixed convection, Int. Commun. Heat Mass Transf. 159 (2024) 107987.
[5] G. de Vahl Davis, Natural convection of air in a square cavity: a bench mark numerical solution, Int. J. Numer. Methods Fluids 3 (3) (1983) 249–264.
[6] T. Basak, S. Roy, A. Balakrishnan, Effects of thermal boundary conditions on natural convection flows within a square cavity, Int. J. Heat Mass Transf. 49 (23–24) (2006) 4525–4535.
[7] N.H. Hamza, et al., Analysis of double-diffusive hydrothermal flow in a domestic stack: the effect of side walls patterns, Heat Transf. 53 (2) (2024) 707–732.
[8] N. Hdhiri, et al., Natural convection study with internal heat generation on heat transfer and fluid flow within a differentially heated square cavity filled with different working fluids and porous media, BioNanoScience 9 (2019) 702–722.
[9] N.S. Gibanov, M.A. Sheremet, Natural convection in a cubical cavity with different heat source configurations, Therm. Sci. Eng. Progr. 7 (2018) 138–145.
[10] S. Aminossadati, B. Ghasemi, The effects of orientation of an inclined enclosure on laminar natural convection, Int. J. Heat Technol. 23 (2) (2005) 43–49.
[11] M.A. Alomari, et al., A comprehensive numerical analysis of heat transfer enhancement in NEPCM-water mixtures using oscillating fin and oriented magnetic fields, Int. Commun. Heat Mass Transf. 161 (2025) 108455.
[12] N. Biswas, et al., Influence of heater aspect ratio on natural convection in a rectangular enclosure, Heat Transf. Eng. 37 (2) (2016) 125–139.
[13] S. Dutta, A.K. Biswas, S. Pati, Analysis of natural convection in a rhombic enclosure with undulations of the top wall–a numerical study, Int. J. Ambient Energy 43 (1) (2022) 87–97.
[14] H. Cui, F. Xu, S.C. Saha, A three-dimensional simulation of transient natural convection in a triangular cavity, Int. J. Heat Mass Transf. 85 (2015) 1012–1022.
[15] M. Sheremet, T. Grosan, I. Pop, Natural convection in a triangular cavity filled with a micropolar fluid, Int. J. Numer. Methods Heat Fluid Flow 27 (2) (2017) 504–515.
[16] M. Hatami, D. Song, D. Jing, Optimization of a circular-wavy cavity filled by nanofluid under the natural convection heat transfer condition, Int. J. Heat Mass Transf. 98 (2016) 758–767.
[17] S.M. Mirabedin, F. Farhadi, Natural convection in circular enclosures heated from below for various central angles, Case Stud. Therm. Eng. 8 (2016) 322–329.
[18] M. Hasanuzzaman, et al., Magnetohydrodynamic natural convection in trapezoidal cavities, Int. Commun. Heat Mass Transf. 39 (9) (2012) 1384–1394.
[19] I.V. Miroshnichenko, et al., MHD natural convection in a partially open trapezoidal cavity filled with a nanofluid, Int. J. Mech. Sci. 119 (2016) 294–302.
[20] A.M. Hassan, et al., Numerical analysis of MHD combined convection for enhanced CPU cooling in NEPCM-filled a trapezoidal cavity, Int. Commun. Heat Mass Transf. 159 (2024) 108343.
[21] M. Sheikholeslami, et al., A study of natural convection heat transfer in a nanofluid filled enclosure with elliptic inner cylinder, Int. J. Numer. Methods Heat Fluid Flow 24 (8) (2014) 1906–1927.
[22] T. Tayebi, H.F. Öztop, A.J. Chamkha, Natural convection and entropy production in hybrid nanofluid filled-annular elliptical cavity with internal heat generation or absorption, Therm. Sci. Eng. Progr. 19 (2020) 100605.
[23] Q. Islam, et al., Natural convection heat transfer within octagonal enclosure, Int. J. Eng. 23 (1) (2010) 1–10.
[24] H. Roshani, et al., The effect of magnetic field on the heat transfer in the porous medium octagonal cavity with Cassini oval barriers, Case Stud. Therm. Eng. 56 (2024) 104194.

[25] M. Mansour, M. Bakier, R.S.R. Gorla, Natural convection in vertical I-shaped nanofluid-filled enclosures, J. Nanofluids 2 (3) (2013) 221–230.
[26] A. Malekpour, N. Karimi, A. Mehdizadeh, Magnetohydrodynamics, natural convection, and entropy generation of CuO–water nanofluid in an I-shape enclosure—a numerical study, J. Therm. Sci. Eng. Appl. 10 (6) (2018) 061016.
[27] M. Mansour, S.E. Ahmed, M. Bakier, Free convection in H-shaped enclosures filled with a porous medium saturated with nanofluids with mounted heaters on the vertical walls, Special Top. Rev. Porous Media Int. J. 4 (4) (2013).
[28] Z. Li, et al., Mixed convection of non-Newtonian nanofluid in an H-shaped cavity with cooler and heater cylinders filled by a porous material: two phase approach, Adv. Powder Technol. 30 (11) (2019) 2666–2685.
[29] A. Abdulkadhim, et al., Magnetohydrodynamics hybrid nanofluid in H-wavy enclosure: natural convection and entropy generation, J. Therm. Anal. Calorim. 2024 (2024) 1–21.
[30] D.R. Vyas, Natural convection of nanofluids in inclined e-shaped enclosures, Am. J. Heat Mass Transf. 4 (1) (2017) 25–39.
[31] Z.A. Raizah, S.E. Ahmed, A.M. Aly, ISPH simulations of natural convection flow in E-enclosure filled with a nanofluid including homogeneous/heterogeneous porous media and solid particles, Int. J. Heat Mass Transf. 160 (2020) 120153.
[32] F.Q. Al-Daamee, N.H. Hamza, Numerical investigation of thermal and entropy generation characteristics in a sinusoidal corrugated channel under the influence of sinusoidal wall temperature, Int. J. Thermofluids 22 (2024).
[33] R.U. Haq, et al., MHD natural convection flow enclosure in a corrugated cavity filled with a porous medium, Int. J. Heat Mass Transf. 121 (2018) 1168–1178.
[34] F. Selimefendigil, H.F. Öztop, Magnetohydrodynamics forced convection of nanofluid in multi-layered U-shaped vented cavity with a porous region considering wall corrugation effects, Int. Commun. Heat Mass Transf. 113 (2020) 104551.
[35] A. Bozhko, M. Kuchukova, G. Putin, The influence of external uniform magnetic field on convection in magnetic fluid filling a spherical cavity, Magnetohydrodynamics 49 (1) (2013) 161–168.
[36] M. Sheikholeslami, M. Gorji-Bandpy, Free convection of ferrofluid in a cavity heated from below in the presence of an external magnetic field, Powder Technol. 256 (2014) 490–498.
[37] K.M. Gangawane, Effect of angle of applied magnetic field on natural convection in an open ended cavity with partially active walls, Chem. Eng. Res. Design 127 (2017) 22–34.
[38] D.D. Dixit, A. Pattamatta, Effect of uniform external magnetic-field on natural convection heat transfer in a cubical cavity filled with magnetic nano-dispersion, Int. J. Heat Mass Transf. 146 (2020) 118828.
[39] K. Ramesh, et al., Numerical solutions and stability analysis of hybrid Casson nanofluid flow with MHD and heat transfer effects, ZAMM-Journal of Applied Mathematics and Mechanics/Zeitschrift für Angewandte Mathematik und Mechanik 2024 (2024) e202301041.
[40] M.G. Reddy, K. Ramesh. Nonlinear Radiative Falkner–Skan flow of hydromagnetic nanofluid over a wedge with arrhenius activation energy, Mathematical Modelling of Fluid Dynamics and Nanofluids, Mathematical Modelling of Fluid Dynamics and Nanofluids, 2024, pp. 475–494.
[41] K.J.M.i.E.S.N.T. Ramesh, Technologies, and applications, thermal radiation effects on the fundamental flows of a Ree–Eyring hydromagnetic fluid through porous medium with slip boundary conditions, Mathematics in Engineering Sciences: Novel Theories, Technologies, and Applications (2019) 205.
[42] S. Gajbhiye, A. Warke, R.J.H.T. Katta, Heat transfer and fluid flow analysis of non-Newtonian fluid in a microchannel with electromagnetohydrodynamics and thermal radiation, Heat Transf. 51 (2) (2022) 1601–1621.
[43] Y. Abdollahzadeh, et al., Modeling and simulation of nanofluid in low Reynolds numbers using two-phase Lattice Boltzmann method based on mixture model, Chem. Eng. Res. Des. 192 (2023) 402–411.
[44] C. Qi, et al., Natural convection of composite nanofluids based on a two-phase lattice Boltzmann model, J. Therm. Anal. Calorim. 141 (2020) 277–287.
[45] C. Qi, et al., Two-phase lattice Boltzmann simulation of the effects of base fluid and nanoparticle size on natural convection heat transfer of nanofluid, Int. J. Heat Mass Transf. 105 (2017) 664–672.
[46] F.S. Oueslati, R. Bennacer, M.El ganaoui, Analytical and numerical solution to the convection problem in a shallow cavity filled with two immiscible superposed fluids, Int. J. Therm. Sci. 90 (2015) 303–310.
[47] Q.S. Liu, G. Chen, B. Roux, Thermogravitational and thermocapillary convection in a cavity containing two superposed immiscible liquid layers, Int. J. Heat Mass Transf. 36 (1) (1993) 101–117.
[48] A. Ouahouah, N. Labsi, Y.K. Benkahla, Marangoni convection flow of two immiscible fluids in an open cavity, Desalination Water Treat. 279 (2022) 152–159.
[49] M. Salari, E.H. Malekshah, M.H. Esfe, Three dimensional simulation of natural convection and entropy generation in an air and MWCNT/water nanofluid filled cuboid as two immiscible fluids with emphasis on the nanofluid height ratio's effects, J. Mol. Liq. 227 (2017) 223–233.
[50] M. Haque, M.J.I.J.o.T. Alam, Natural convective heat transfer of Al2O3-Cu/water hybrid nanofluid in a rectotrapezoidal enclosure under the influence of periodic magnetic field, Int. J. Thermofluids. 22 (2024) 100661.
[51] M. Izadi, M.A. Sheremet, S.J.C.J.o.P. Mehryan, Natural convection of a hybrid nanofluid affected by an inclined periodic magnetic field within a porous medium, Chin. J. Phys. 65 (2020) 447–458.
[52] T. Islam, et al., Impact of non-uniform periodic magnetic field on unsteady natural convection flow of nanofluids in square enclosure, Fractal and, Fractional 6 (2) (2022) 101.
[53] A.M. Hassan, et al., Numerical analysis of free convection under the influence of radiation and inclined MHD in a triangular cavity filled with hybrid nanofluid and a porous fin, Int. J. Thermofluids. (2024) 100843.
[54] M. Salari, E.H. Malekshah, M.H. Malekshah, Natural convection in a rectangular enclosure filled by two immiscible fluids of air and Al2O3-water nanofluid heated partially from side walls, Alex. Eng. J. 57 (3) (2018) 1401–1412.
[55] M. Hatami, et al., Optimization of a lid-driven T-shaped porous cavity to improve the nanofluids mixed convection heat transfer, J. Mol. Liq. 231 (2017) 620–631.
[56] M. Salari, E.H. Malekshah, M.H.J.A.E.J. Malekshah, Natural convection in a rectangular enclosure filled by two immiscible fluids of air and Al2O3-water nanofluid heated partially from side walls, Alex. Eng. J. 57 (3) (2018) 1401–1412.
[57] R.A. Hussein, A.M. Hassan, R.H. Hameed, Mixed convection heat transfer in a partial porous layered split lid-driven wavy wall cavity with Cu–H2O nanofluid, Numer. Heat Transf. Part B Fundam. (2024) 1–27.
[58] T. Basak, et al., Natural convection in a square cavity filled with a porous medium: effects of various thermal boundary conditions, Int. J. Heat Mass Transf. 49 (7–8) (2006) 1430–1441.
[59] J.N. Reddy. An Introduction to the Finite Element Method, ASME, J. Pressure Vessel Technol.27, 1993, p. 14.
[60] M. Ghalambaz, M. Sabour, I. Pop, Free convection in a square cavity filled by a porous medium saturated by a nanofluid: viscous dissipation and radiation effects, Eng. Sci. Technol. Int. J. 19 (3) (2016) 1244–1253.
[61] T. Basak, et al., Natural convection in a square cavity filled with a porous medium: effects of various thermal boundary conditions, Int. J. Heat Mass Transf. 49 (7) (2006) 1430–1441.
[62] J.N. Reddy, Introduction to the Finite Element Method, McGraw-Hill Education, 2019.